THE IMPACT OF PROPPANT GRAIN SIZE DISTRIBUTION ON

FRACTURE CONDUCTIVITY IN SHALE FORMATIONS

A Thesis

by

ALLYX MICHELLE COPELAND

Submitted to the Office of Graduate and Professional Studies of
Texas A&M University
in partial fulfillment of the requirements for the degree of

MASTER OF SCIENCE

Chair of Committee,	Ding Zhu
Committee Members,	A. Daniel Hill
	Marcelo Sanchez
Head of Department,	Jeff Spath

August 2020

Major Subject: Petroleum Engineering

ABSTRACT

To further improve a propped fracture's performance, this study investigated how the distribution of a proppant's grain size can affect fracture conductivity. The goals of this project were to quantify and explain the impact uniform and non-uniform grain size distribution for 100-mesh proppants have on the propped fracture conductivity measured for fractured shale core samples.

Eagle Ford core collected from an outcrop and Meramec core extracted from downhole conditions were tested in this study. The cores were fractured and propped by two different proppant types: a non-uniformly distributed 100-mesh proppant provided by Marathon Oil and a created 100-mesh proppant with a uniform grain size distribution. To create this proppant, the provided 100-mesh was sieved and the grains collected by the No. 120 pan were used.

A Modified API fracture conductivity cell was utilized to measure the fracture conductivity when dry nitrogen was pumped through the propped fractures. Before the Eagle Ford and Meramec cores were test, preliminary experiments were implemented to analyze and compare the two proppant types. For each proppant, density, specific gravity, void ratio, and porosity were determined.

Although the scope of this investigation was focused on proppant, additional work was done to evaluate the core because rock characteristics and mineralogy also affect fracture conductivity. For all samples, the top and bottom fracture surfaces were scanned using a fracture surface laser profilometer. The data collected by the profilometer was used to model fracture surface topography and quantify the surface volume changes before and after the fracture conductivity

experiments. The relationships between proppant embedment, proppant grain size distribution, rock mineralogy, and fracture surface topography were discussed.

From the results yielded in this study, it was concluded that proppant gradation does impact fracture conductivity. Consistently, for the different shale samples, a proppant with grains the same size and shape yielded higher fracture conductivity values than the proppant with a well distributed grain size. The results also indicated poorly distributed proppant was more susceptible to self-channeling than the well distributed proppant with non-uniform grain size distribution.

Therefore, this study offers an insight into the effect proppant grain size distribution has on fracture conductivity. This study also presents the detailed methodology for quantifying fracture conductivity in the laboratory setting.

DEDICATION

I would like to dedicate this work to my mother and late father. He may be gone, but he is not forgotten. I owe all that I am and all that I have learned to them. Without their unwavering support, I would not be where I am today.

ACKNOWLEDGEMENTS

CONTRIBUTORS AND FUNDING SOURCES

NOMENCLATURE

e	Void ratio
dP/dL	Pressure gradient across the proppant pack (psi/ft)
SG	Specific gravity
ϕ	Porosity (%)
q	Volumetric flow rate (ft/s)
A	Cross-sectional area (in^2)
β	Forchheimer inertial factor
w_f	Fracture width (thickness) (in)
h_f	Fracture height (width) (ft)
k_f	Fracture permeability (md)
L	Sample length (ft)
M_g	Molecular mass (kg/mol)
$\dot{M}$	Mass flow rate (kg/min)
P_1	Upstream pressure (psi)
P_2	Downstream pressure (psi)
P_{cell}	Cell pressure (psi)
R	Universal gas constant (J/mol K)
T	Temperature (K)
v	Fluid velocity (m/s)
Z	Gas compressibility factor
ρ_f	Density of fluid (kg/m^3)
μ	Viscosity of fluid (cP, Pa-s)

Δp	Differential pressure (psi)
C_f	Fracture conductivity (md-ft)
API	American Petroleum Institute
ISO	International Organization for Standardization
ASTM	American Society for Testing and Materials
RTV	Room Temperature Vulcanizing
XRD	X-Ray Diffraction

TABLE OF CONTENTS

LIST OF FIGURES

LIST OF TABLES

1. INTRODUCTION

1.1 Background

The oil and gas industry had relied on conventional reservoirs for decades and these high quality and profitable reservoirs were slowly becoming obsolete. As time and technology progressed, the industry began to shift their efforts towards extracting hydrocarbons from the source rock, where the hydrocarbons originate from, in conventional reservoirs. These source rocks are fine-grain, clastic sedimentary rocks commonly referred to as shales.

One of the many methods employed to stimulate the poorly-permeated shale rocks for better productivity is hydraulic fracturing. This method greatly increases the contacted reservoir area and, as a result, increases the economic lives of some wells (Daniel and White, 1980). At pressures above the formation's fracture pressure, viscous, proppant-loaded fluids are injected into the fractured shale formation. The proppant in the injection fluid helps prevent the induced fractures from closing and allows the hydrocarbons to flow through a more conductive channel.

A useful parameter calculated to predict and evaluate the success of a propped fracture job is fracture conductivity. In 1973, Cooke found that an increase in fracture conductivity by a factor of ten can lead to a fracture treatment that is up to six times as effective (Cooke, 1973). For decades, researchers have developed, modified, and improved the laboratory procedures for quantifying this parameter in propped shale core. To be put simply, fracture conductivity is the product of fracture width and the apparent proppant pack permeability (Cooke, 1973). It has been used by many to explain how well a fluid is able to move through a fracture. High conductivity values are preferable because, in this case, there is more space, or fracture width, for the fluid to travel from the reservoir into the wellbore.

The growing popularity of hydraulic fracturing has led to a variety of conductivity tests being performed on downhole core from many diverse formations. Additionally, due to the increased use of proppant in the field to enhance a fracture's performance, many fracture conductivity tests have been done using a variety of proppant sizes and concentrations. The following work presented in this thesis is a continuation of the ongoing systemic investigation on fracture conductivity in shale formations, specifically the Eagle Ford and Meramec formations.

1.2 Literature Review

Both the industry and academia have expended countless efforts analyzing and modeling the Meramec and Eagle Ford formations. There have been many studies done to explain and improve hydraulic fracturing through the quantification of fracture conductivity in the laboratory setting. This section provides a review of a few of these studies related to the work performed in this thesis.

1.2.1   Hydraulic Fracturing in Shale Formations

Although fracturing can be traced back to the 1860s, the first experimental hydraulic fracturing treatment was performed by Stanolind Oil in the Hugoton gas field in Grant Country, Kansas, in 1947. Stanolind Oil injected 1,000 gallons of naphthenic-acid-and-palm-oil-thickened gasoline, followed by a gel breaker to stimulate a gas-producing limestone formation at 2,400 feet (Montgomery and Smith, 2010). Their "hydrafrac" method did not impact the deliverability of their well, however, it did jump start the industry's interest and later reliance on hydraulic fracturing.

To improve a hydraulically fractured formation's deliverability, researchers introduced the application of proppant to hinder fracture closure in a formation's fracture network. The first fracturing treatment utilized river sand as a proppant (Montgomery and Smith, 2010).

Throughout the years, a wide range of materials, such as plastic pellets and Indian glass beads, have been used to try to increase performance in shales with varying success (Montgomery and Smith, 2010). Wylie concluded for a given particle size under ideal conditions, sand had the highest conductivity followed by taconite, glass, and finally coal, which did not result in any measurable conductivity (Wylie, 2018).

Around the world, researchers and production engineers are continuing to further their understanding and improve proppant application because the creation of propped-fracture conductivity, that is sustainable at closure stresses during production, is critical to the success of hydraulically fractured treatments in unconventional reservoirs (Enriquez-Tenorio et al., 2016). With this being said, hydraulic fracturing techniques evolve with technology and vary amongst operators and the shale formations they are working to stimulate. Proppant placing with slickwater, linear gel, and hybrid treatments are a few examples of the design methods employed in the field.

The slickwater method uses water mixed with friction reducers to transport the proppant. However, water's low viscosity can limit the proppant's transport throughout the fracture and, thereby, reducing the fracture's performance. Proppant transport is an important mechanism to consider in the design process. If the proppant is not transported deep into the fracture, the fracture will close and restrict the flow of hydrocarbons traveling from the formation. Manipulating the viscosity of the fracture fluid and understanding what characteristics of proppant affect proppant transport can help improve the performance. Palisch concluded that while proppant size is much more important than proppant density, both factors, along with fluid rate and viscosity, affect proppant transport (Palisch et al., 2010).

1.2.2   Parameters Affecting Propped Fracture Conductivity

Cooke, in the 1970s, pioneered proppant pack conductivity research. He studied the effect of environment (fluid present and temperature) on the conductivity of brittle proppant under stress and the effect of flow rate (derived from Darcy's Law) on the flow resistance of proppant (Cooke, 1973). He, and the researchers who followed in his footsteps, proved proppant size, shape, distribution, physical properties, and quantity should all be considered for they impact the effectiveness of a treatment (Wiley, 2018).

Misunderstood or wrongly applied understandings of proppant performance happen. Duenckel et al. (2017) presented a few of these cases and offered assistance to practicing engineers in well diagnostics and stimulation design. For the past 30 years, researchers, such as Duenckel, at the Stim-Lab Proppant Consortium have engaged in a continuous program that builds their knowledge and understanding of the behavior of all types of proppants used in hydraulic fracturing. Arguably, no other body of knowledge about proppants exist that compares in extent and detail with that accumulated by the Consortium (Duenckel et al., 2017). After three decades of research, they conclude the permeability of a specific size and type of proppant at reservoir conditions is impacted by a number of factors including closure stress, proppant concentration, fracture fluid damage, time at stress, the fluid velocities, reservoir rock properties, and others.

In 2017, Mittal et al. also extensively studied the effect of proppant size, proppant crushing, fines migration, rock mineralogy and fluid chemistry on long-term fracture conductivity. He concluded fracture conductivity is dependent on proppant size and the pH of the flowing solution. Using Eagle Ford shale samples, his experiments found the proppant-pack permeability

for 60/100 sand drops dramatically within a few hours and the 20/40 proppant permeability is double the permeability of 60/100 sand even after 10 days of testing (Mittal et al., 2017).

Prior to Mittal's work, Kamenov's quantified the propped fracture conductivity for core extracted from the Barnett shale formation and his results were comparable to Mittal's. He concluded propped fracture conductivity is proppant-dominated and it is less affected by the degree of fracture surface roughness or displacement (Kamenov, 2013). He also found, within the limits of his experimental design, the conductivity of propped fractures increases with larger proppant size and higher proppant loading concentrations.

Enriquez-Tenorio et al. (2016) found the propped fracture conductivity of Eagle Ford shale samples primarily depended on proppant size and loading and were less dependent on the rock properties. His results proved that propped and unpropped conductivities decline exponentially with closure stress. Furthermore, Enriquez-Tenorio concluded conductivity was positively related to rock brittleness and inversely related to Poisson's ratio (Enriquez-Tenorio et al., 2016).

1.2.3 Fracture Conductivity Measurement Procedure and Quantification

There are two methods that can be utilized to quantify fracture conductivity in the laboratory setting; the standard International Organization for Standardization (ISO) conductivity test and the modified ISO conductivity test. The standard ISO 13503-5:2006(E) was designed to establish standard experimental conditions and procedures for evaluating the conductivity of proppants under laboratory conditions (Zhang et al., 2014). Without considering most realistic conditions, the standard ISO conductivity procedures and experimental setup are used primarily for analyzing and comparing the performance of various proppants and for creating a baseline fracture conductivity value.

A modified version of this test was used for this project because the procedures can be changed to reflect more realistic conditions. This modified American Petroleum Institute (API) test allows researchers to test shale core samples in a modified API conductivity cell that is able to accommodate for 3x thicker samples, while maintaining pressure (i.e. very minimal pressure leakoff). The design of this cell was derived from the standard API fracture conductivity cell detailed in API RP 61 (1989).

Furthermore, the modified API cell design enables researchers to pump dry gas, fresh water, wet gas, different concentrations of brine solutions, oil, and multiphase fluid through a variety of proppant loading concentrations. Zhang et al., in 2014, used the modified API conductivity test to measure the fracture conductivity of propped and unpropped core samples from the Barnett, Eagle Ford, and the Fayetteville shale formations by flowing dry nitrogen (Zhang et al., 2014). Dry nitrogen was also used for this project because, unlike the standard's recommended 2% KCl, it does not change the integrity of the shales. If needed, the samples could be retested.

1.2.4   Proppant Behavior and Performance Evaluation

To help predict and improve a fracture's conductivity, it is beneficial to understand how the proppant behaves after it is pumped into the fracture under the high pressure conditions. In order to explain how a proppant may behave in the fracture, it is beneficial to determine the properties and characteristics of the proppant being implemented. Researchers have concluded an ideal fracture treatment should consist of large, spherical, uniformly-sized proppant particles with a strength that can withstand the high overburden stresses.

Larsen and Smith (1985) concluded the sphericity and roundness of the proppant grains in the proppant pack can both positively and negatively impact permeability and conductivity. They

defined roundness as the smoothness of a grain's surface, or the lack of rough edges, and

sphericity as the degree a sand grain resembles a sphere (Larsen and Smith, 1985). Higher

conductivity values are yielded when spherical and round proppant grains are used. The pore

space, or void space, between the grains increases when the grains' sphericity increases. When

the void space increases, then, as **Figure 1** depicts, permeability also increases.
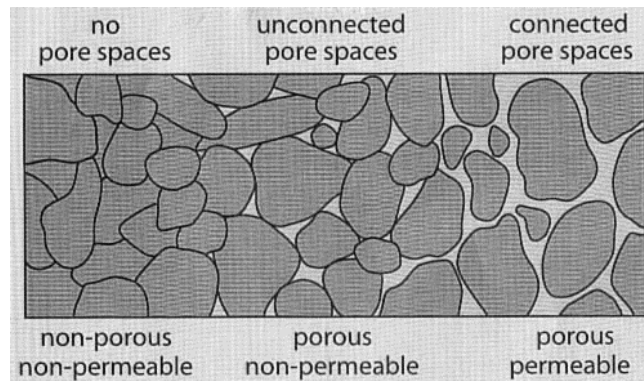
Figure 1. Relationship between pore space and permeability (adapted from the University of Nebraska Omaha, 2020).

    If a selected proppant cannot withstand the overburden stress causing fracture closure,

proppant crushing can occur, which has a negative impact on fracture conductivity. **Figure 2**

illustrates the stages the proppant may undergo when closure stress is applied to a propped

fracture sample (Zhang, 2014). The fracture conductivity reduces because the fines created from

the crushed proppant can lead to fines migration and embedment (Cooke, 1977). When proppant

embedment occurs, fluids from the reservoir are not able to travel as effectively into the fracture

because the fines clog the pore space.
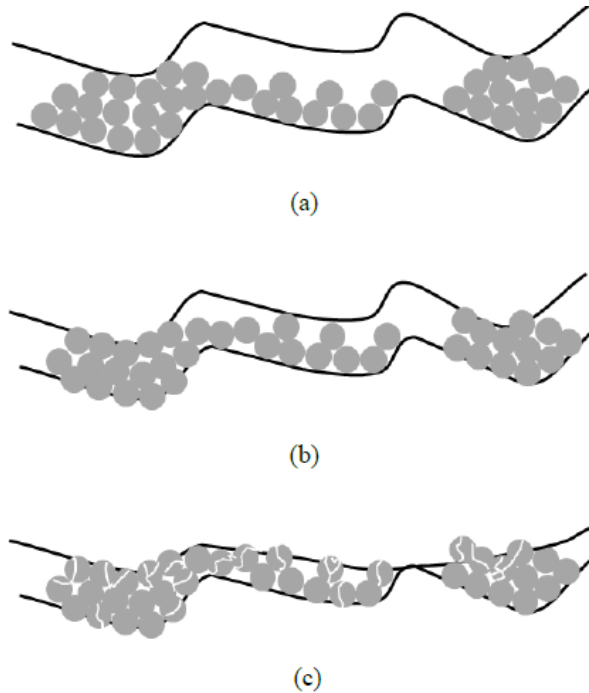
Figure 2. Proppant distribution on a rough shale fracture surface: (a) initial proppant pack with large void space above the proppants, (b) proppant grain rearrangement during the application of closure stress, and (c) at high closure stress, proppants are crushed and the rock creeps (modified from Zhang, 2014).

Proppant self-channeling may also occur and positively impact conductivity in the field and laboratory setting. After the fluid navigates through the proppant, the final proppant distribution on the fracture surface is no longer uniform. With this phenomena, proppant is absent in some locations along the fracture surface. At these locations, highly conductive channels are able to form. Rates of injection during hydraulic fracturing, fluid viscosity, and fracture surface attributes all allow for channeling to occur because these factors directly influence proppant transport and distribution (Raimbay et al., 2015; Gomaa et al., 2016).

When testing the fracture conductivity of Eagle Ford outcrop core, Guerra experienced this proppant phenomena, as shown in **Figure 3**. He introduced the idea that there may be an

optimum initial proppant concentration that could result in the highest channeling behavior for a

particular fracture surface (Guerra, 2019).
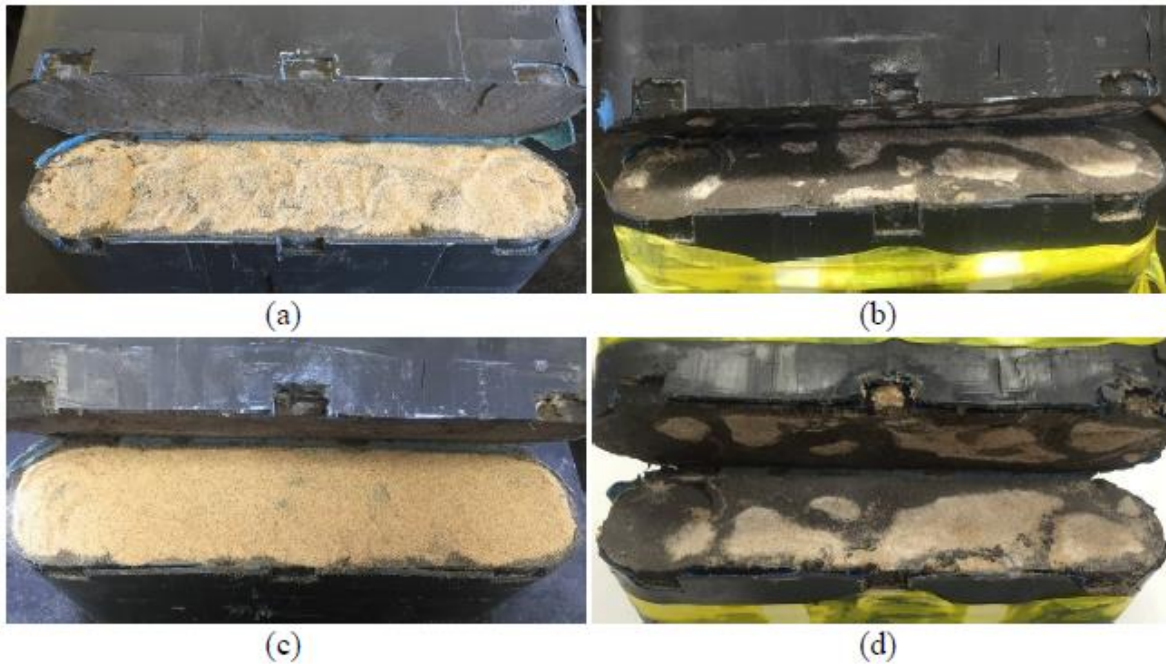
Figure 3. The distribution of proppant along the fracture surface for Fracture Conductivity Test Sample EF-1: (a) and (b) proppant loading of 0.1 lbm/ft² 100-mesh sand before fracture conductivity test and resulting proppant distribution after fracture conductivity test; (c) and (d) proppant loading of 0.2lbm/ft² 100-mesh sand before fracture conductivity test and resulting proppant distribution after fracture conductivity test (modified from Guerra, 2019).

Guerra also concluded the following may have instigated self-channeling proppant:

- A high velocity gas flow at low closure stresses without the installment of a

  screen immediately after the fracture conductivity cell.

- The uneven fracture surface may have allowed for proppant to roll and shift from

  the surface peaks to the surface valleys.

- A low proppant concentration (0.1-0.3lbm/ft²) and a relatively small proppant

  grain size (100-mesh proppant).

9

1.3 Problem Description, Objectives, and Significance

This study aimed to investigate how inconsistencies in the grain size of the proppant being provided by manufacturers can impact fracture conductivity. The goals of the study were to quantify and explain the impact industry-provided proppant and that same proppant manually sieved to the actual advertised mesh size has on fracture conductivity and overall performance.

The following objectives were accomplished:

(1) Improve and perform laboratory procedures used to measure propped shale fracture conductivity.

(2) Measure the fracture conductivity of shale core from the Eagle Ford and Meramec formations propped by 100-mesh proppants with different grain size distributions.

(3) Investigate and quantify the impact of proppant grain size distribution on conductivity.

The results from this study expand and elevate the industry's understanding of proppant application. Furthermore, the application of proppant with small mesh size in the field is expanding. For example, smaller proppant, such as 100-mesh, is thought to be capable of propping the natural fracture network in shale reservoirs and maximizing the conductive fracture contact with the formation (Zhu and Hill, 2013). The insights gained from the work performed can be used to optimize a fracturing job's design and, ultimately, increase production.

1.4 Experimental Approach

To achieve the objectives established, the following steps were performed:

(1) Collect Eagle Ford shale samples.

(2) Determine the provided 100-mesh proppant's grain size distribution.

10

(3) Create a 100-mesh proppant with a grain size between Sieve No. 100 and Sieve No. 120.

(4) Take microscopic images of the two proppants used.

(5) Scan the top and bottom fracture surfaces with a laser profilometer.

(6) Prepare the shale samples for the conductivity experiments.

(7) Run conductivity experiments.

(8) Scan the top and bottom fracture surfaces again.

(9) Perform calculations.

(10) Analyze the results.

2. EXPERIMENTAL DESIGN AND METHODOLOGY

2.1 Introduction

This section explains how the samples were prepared for the fracture conductivity test and the methodology behind the procedures and equipment used. Some of the methods applied are comparable to the previous work done by Winner (2018), Guerra (2019), and Zhang (2014). Similar to the samples used in Winner's thesis, Marathon Oil provided unpreserved downhole Meramec shale core from their Rosemary 4-H well located in Oklahoma, U.S.A. The Eagle Ford shale core samples were purchased from Kochurek Industries.

Four Meramec shale core and four Eagle Ford shale core were tested. Samples No. 1 through 4 were cored at depths between 9,640 ft. and 9,730 ft. in the Meramec formation. Samples No. 5 through 8 were extracted from the upper portion of Unit B in **Figure 4**, an image of an Eagle Ford outcrop located in Terrell County, Texas.
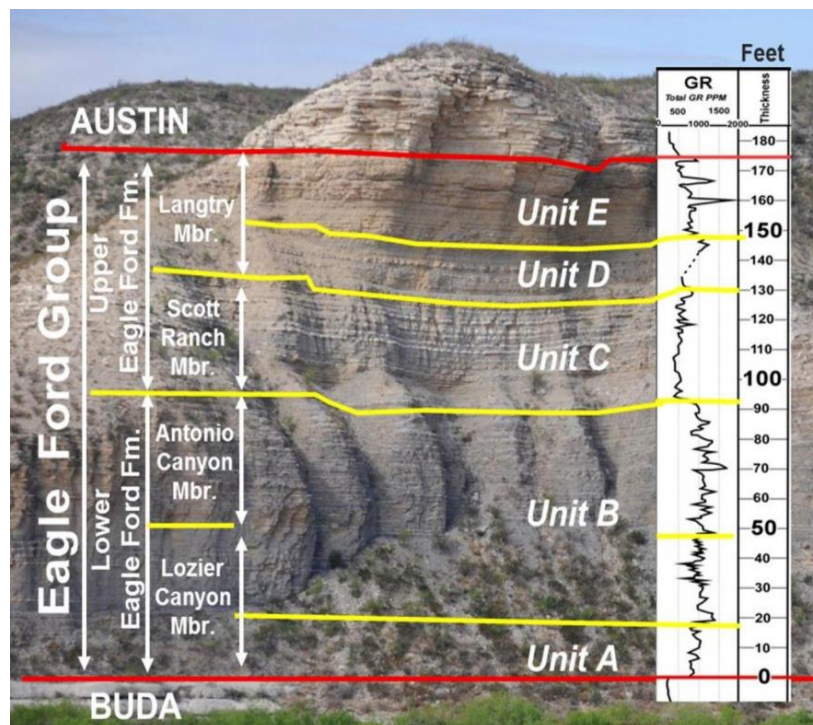
Figure 4. The Eagle Ford outcrop, where Samples No. 5-8 were sourced, in South Texas (Donovan et al., 2012).

The locations in Oklahoma and Texas where the cores were acquired are notated in

Figure 5.
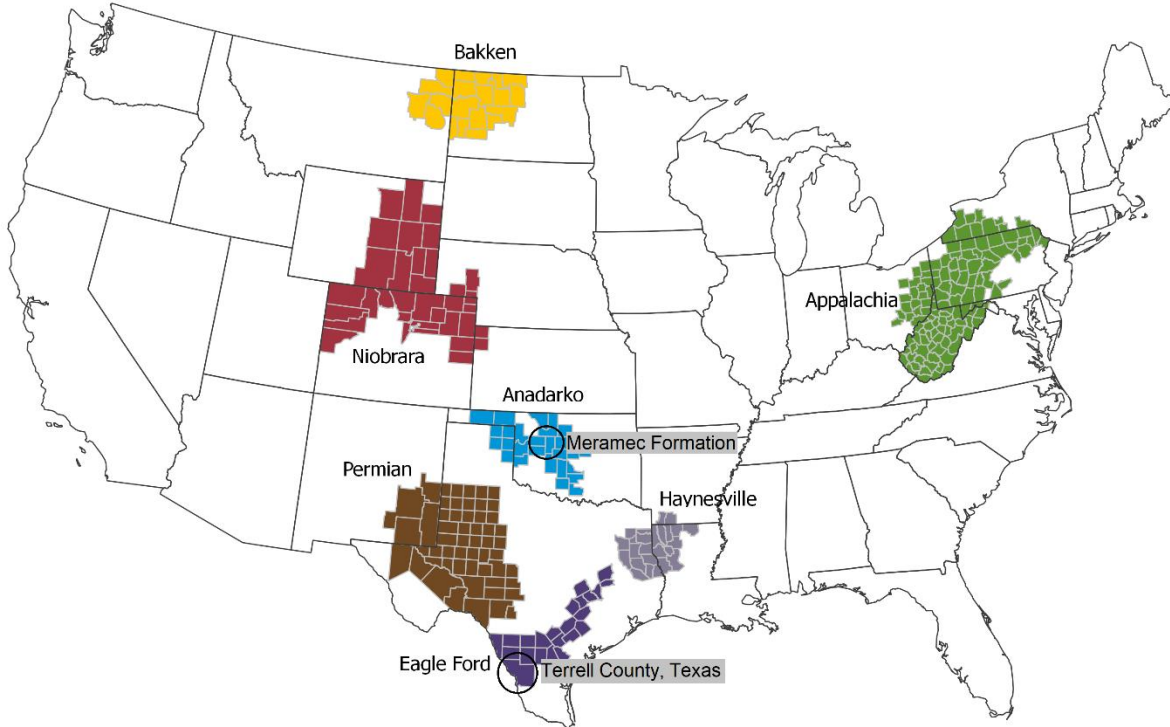
Source: U.S. Energy Information Administration

Figure 5. The two locations where the shale cores were collected in Texas and Oklahoma, as well as, the seven major shale plays in the United States (modified from United States Energy Information Administration, 2020).

2.2 Proppant Distributions and Analysis

Four samples, two using Eagle Ford core and two using Meramec core, were made with a 100-mesh proppant provided by Marathon Oil from their Oakwood 100-Mesh Silo #5. The provided 100-mesh proppant was sieved using American Society for Testing and Materials standards to establish the average particle distribution (ASTM, 2019). The distribution of the 100-mesh proppant grains can be found in **Figure 6**. Although there is no standard distribution required by the industry, a 100-mesh proppant's grain size is typically expected to range between

the No. 80 sieve and No. 100 sieve. Grains larger than the No. 80 sieve and smaller than the No. 40 sieve are considered a 40/70-mesh proppant.
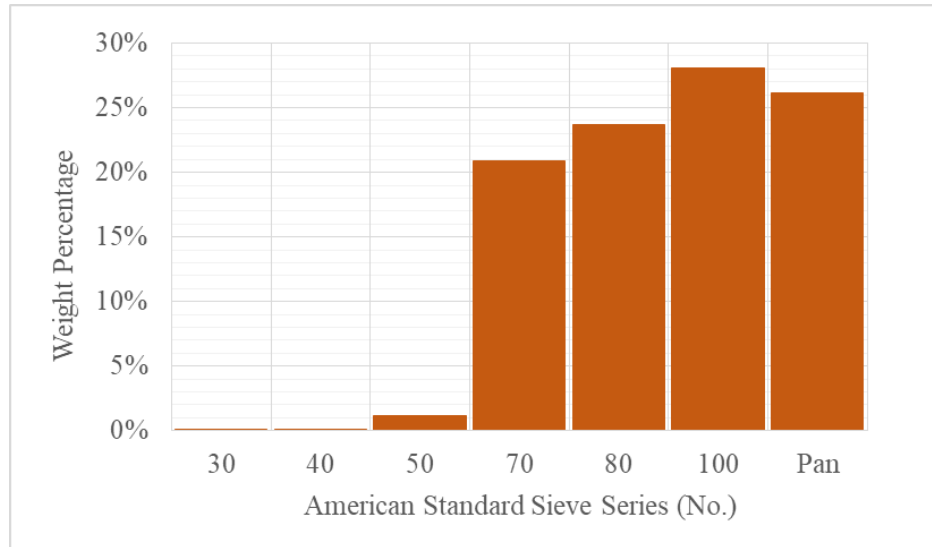
Figure 6. The grain size distribution of the provided 100-mesh proppant.

The remaining four samples were made using the "created" 100-mesh proppant. To create this proppant, a portion of the provided 100-mesh was sieved again and the grains captured by the No. 120 sieve were collected. As shown in **Figure 7**, the provided proppant's grains varied in size and shape, while the created proppant's grains were more consistent in their shape and size.
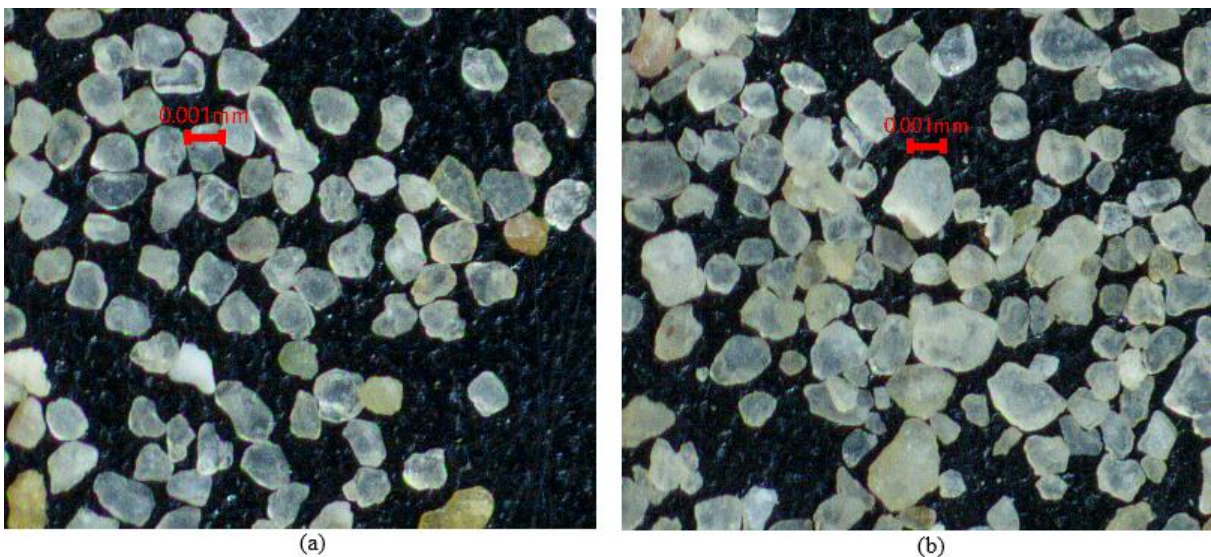
Figure 7. Microscopic images of the proppant grains: (a) created 100-mesh proppant; (b) provided 100-mesh proppant.

Using the microscopic images and sieve analysis, the provided proppant was concluded to be non-uniformly distributed, or well-graded, when compared to the uniformly distributed, or poorly-graded, created proppant using the United Soil Classification System (USGS) presented in the *Engineering Geology Field Manual* (Bureau of Reclamation, 2016). This determination was useful in understanding the pore space between the proppant grains. A well-graded sand, having a good distribution of particle size from large to fine, is relatively less permeable than a poorly-graded sand of a comparable size, because the finer grains will fill the space between the larger particles (U.S. Department of Agriculture, 2012).

The well distributed proppant's pore space was considered smaller than the poorly distributed proppant, and therefore, the poorly distributed created proppant was hypothesized to exhibit more porous behavior with higher conductivity values. A comparison between the ideal examples of well distributed and poorly distributed proppant and their respective pore spaces can be found in **Figure 8**.
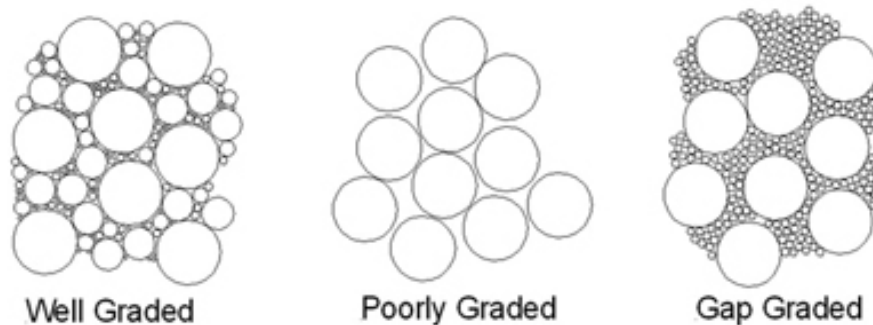
Figure 8. Schematic of well-graded and poorly-graded proppant pore space**.**

In summation, the proppant types used for each sample and their respective core type are displayed in **Table 1.**

Table 1. Core and proppant type for the samples tested.

Sample No.	Core Type	Proppant Type
1	Meramec	Provided 100-Mesh
2	Meramec	Provided 100-Mesh
3	Meramec	Created 100-Mesh
4	Meramec	Created 100-Mesh
5	Eagle Ford	Provided 100-Mesh
6	Eagle Ford	Provided 100-Mesh
7	Eagle Ford	Created 100-Mesh
8	Eagle Ford	Created 100-Mesh

2.2.1 Calculated Proppant Physical Properties

To better understand the differences and similarities between the provided and created proppants, a few physical properties were quantified. These values were used to predict the behavior of each proppant and explain the experimental results.

Using a graduated cylinder and a scale, the densities for both proppant types were determined. 5 ml of each proppant was poured into the clean graduated cylinder and weighed. For a density that represented the proppants as a whole and not only the initial portion collected, six 5 ml collections were individually taken and weighed from both the provided and created proppant bins. For each proppant, an average density was calculated from the six measurements. These average densities calculated and converted from g/ml to g/cm^3 are listed in **Table 2.**

Table 2. Calculated physical properties of the proppants used.

Proppant Type	Density (g/cm^3)	Specific Gravity	Void Ratio	Porosity (%)
Provided	1.48	2.59	0.43	30
Created	1.44	2.64	0.45	31

The specific gravities displayed in **Table 2** were calculated for each proppant type using the following steps:

1) Weigh a clean and dry 1000 ml graduated cylinder.

2) Fill the 1000 ml graduated cylinder with 500 ml of water. Weigh the water and container in grams. Record the weight.

3) Add sand until the water level in the container reaches about 750 ml. Allow the sand to settle. Record the increased weight and exact volume change.

4) Determine the mass of the sand by subtracting the weight of sand and water recorded in Step (3) by the weight of water recorded in Step (2).

5) The specific gravity of the sand is the mass of the sand divided by the exact volume change recorded in Step (2).

Lastly, the void ratios and porosities were calculated using **Eq. 1 and Eq. 2,** respectively.

$$e = \frac{SG - \rho_{sand}}{SG} \tag{1}$$

$$\phi = \frac{e}{e+1} \tag{2}$$

In **Eq. 1**, e is the void ratio, SG is the specific gravity of the sand, and ρ_{sand} is the density of the sand. In **Eq. 2**, ϕ is the porosity. Void ratio for a sand pack is the ratio between the volume of void spaces, or pore spaces, to the volume of sand grains, while porosity is the ratio of the void volume to the total volume, i.e. the volume of void space and sand grains. In regards to fracture conductivity, proppants with high void ratios and porosities are desired.

Based on the calculated values in **Table 2**, in theory, the created proppant should yield higher conductivity values because it is more porous than the provided proppant. However, the closure stresses being applied to the samples during the experiment may discredit this theory because the proppant's integrity can change. Again, the permeability of a specific size and type of proppant at reservoir conditions is impacted by a number of factors, including closure stress and reservoir rock properties (Duenckel et al., 2017).

2.2.2 Calculated Proppant Loading Concentrations

For all eight samples, the proppant concentration used was 0.2 lbm/ft^2 because this was the standard practice Marathon Oil used for their hydraulic fracture treatments in the Meramec Formation. Maintaining consistency between the eight samples during pre-experimental preparation was important. The same mass of proppant was used to prop each sample.

In order to determine the mass of the proppant reflective of a 0.2 lbm/ft^2 loading concentration, the surface area of the fracture was found using the same methodology as Winner (2018). By assuming a planar fracture area, the total fracture surface area of the samples used was 0.0762 ft^2. With the proppant concentration and calculated total surface area, the mass of the proppant required for each sample was determined to be 6.81 g.

2.3 Core Sample Preparation

This section explains how the shale cores were cut, fractured, digitally scanned, and then epoxied. The modeled topography of the fracture surfaces is also provided in this section.

2.3.1 Sample Fracturing

Kochurek Industries cut all core into the dimensions required for the samples to securely fit into the Modified API conductivity cell. Using a method explained by Guerra (2019) and perfected by previous graduate students in the research group, a fracture was induced to create the samples, as shown in **Figure 9.**

Figure 9. The surfaces created by Kochurek Industries using the tension method: (a) fracture surfaces of a Meramec shale sample (Sample No. 2); (b) fracture surfaces of an Eagle Ford shale sample (Sample No.5).

To further guarantee each shale sample fit evenly inside of the cell, two Berea sandstone spacers were glued to the top and bottom of the samples. Most importantly, these spacers allowed the fracture to align with the Modified API cell's sensor ports and the inlet and outlet nitrogen flow lines. The dimensions for the shale and spacers are detailed in **Figure 10.**
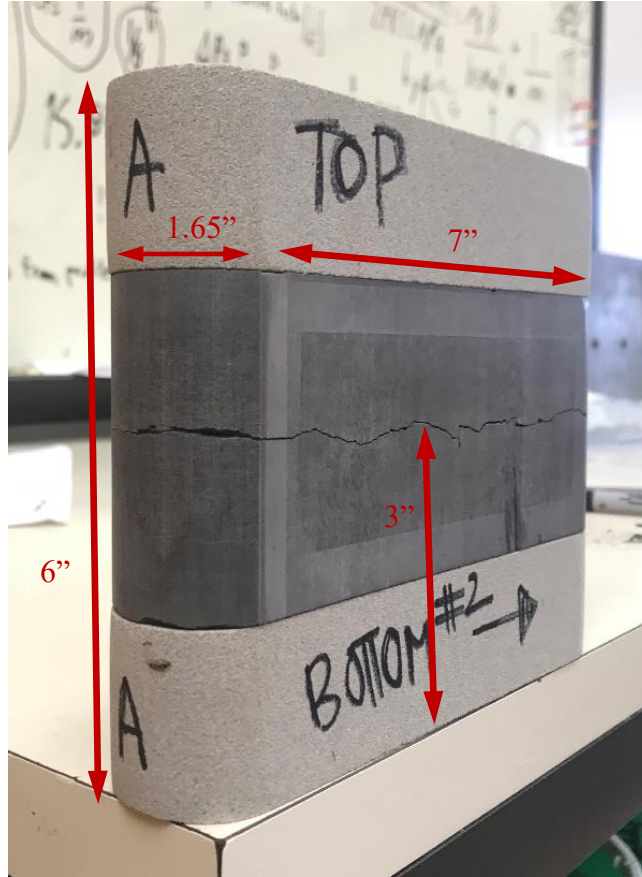
Figure 10. The dimensions of all shale samples used.

2.3.2   Surface Profile Scan

Before the samples were prepared for the fracture conductivity test, the direction of flow

through the fracture was established for each sample. While keeping in mind that the fracture

needs to rest at a height of 3 in. above the cell's bottom piston, the orientation of the sample

placement was determined. The goal was to select the side with the fracture propagating at a

level height to be the front of the sample (i.e. this side of the sample was in contact with the

sensor ports located on the front of the Modified API cell).

With the direction of flow established, a laser profilometer was used to scan the fracture

surfaces before and after the conductivity tests. The equipment and procedure presented by

Winner (2018) was applied with one modification; a measurement interval of 0.05 was used

instead. The laser profilometer equipment moved the sample in both the x- and y-directions, while the laser measured the z-direction, or height, of the sample at a single point (Winner, 2018).

The laser profilometer software outputted a text file with x, y, and z measurements scanned from the fracture surface. A MATLAB program plotted the coordinates and created a 3-dimensional fracture surface profile. The fracture surface profiles before the fracture conductivity experiments for the Meramec shale samples and Eagle Ford shale samples are displayed in **Figures 11 and 12**, respectively.

(a)

(b)

(c)

(d)
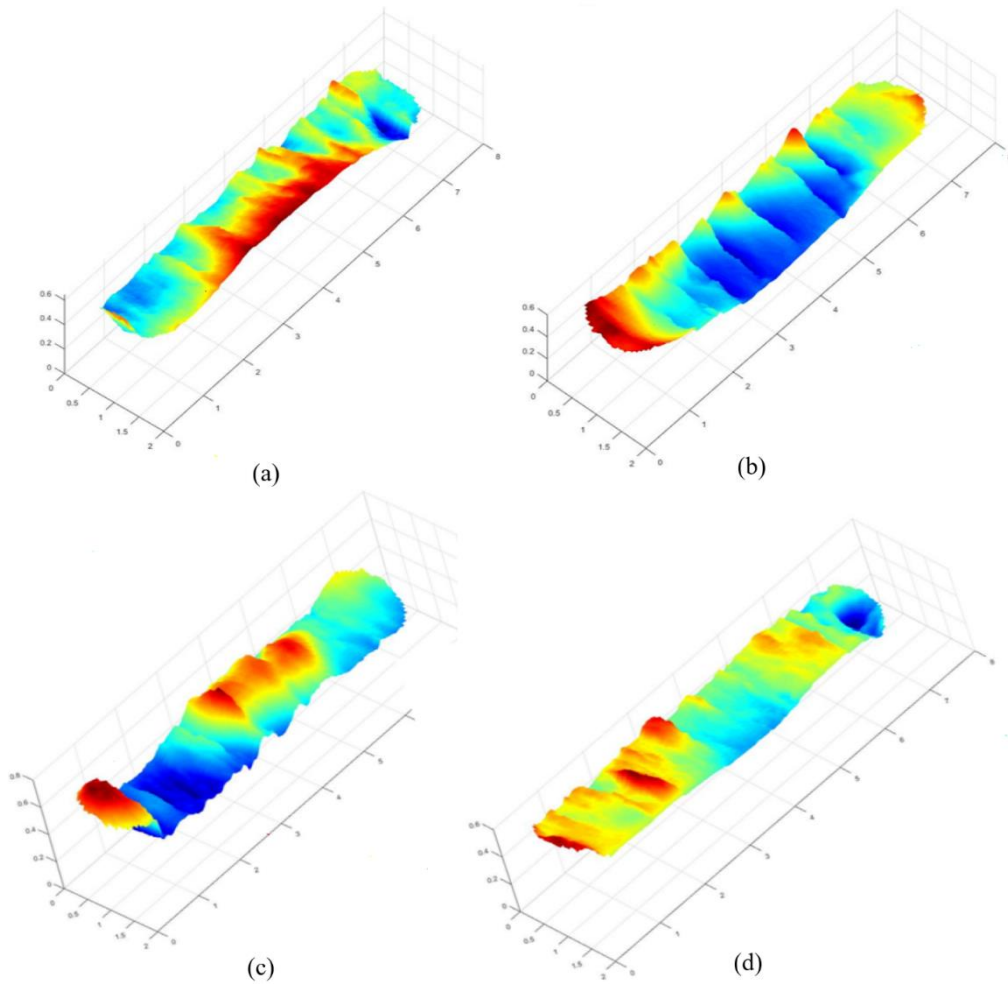
Figure 11. The fracture surface scans of the Meramec core samples: (a) Sample No. 1; (b) Sample No. 2; (c) Sample No. 3; (d) Sample No. 4.

(a)

(b)

(c)

(d)
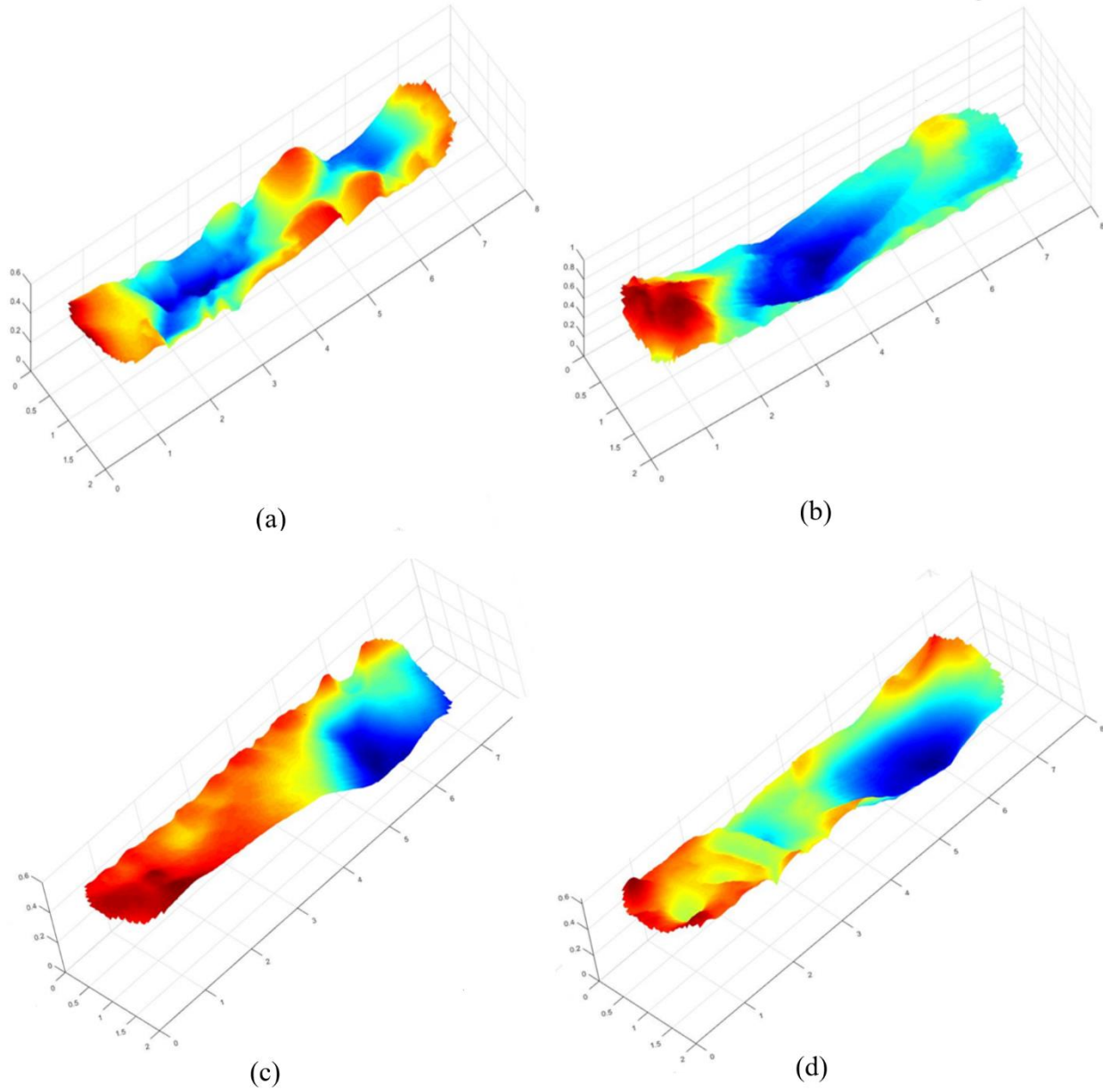
Figure 12. The fracture surface scans of the Eagle Ford core samples: (a) Sample No. 5; (b) Sample No. 6; (c) Sample No. 7; (d) Sample No. 8.

The surface scans show each sample had a unique fracture surface. Using the measurements taken for each sample, MATLAB codes were also utilized to calculate surface volume changes after the experiments. Before the sample was scanned after the conductivity tests, the loose sand was gently brushed away from the fracture surfaces.

By comparing the various surfaces with the fracture conductivity results, the goal was to gain an overall understanding of what truly influenced the calculated fracture conductivities. Using the data from the surface volume change calculations, an attempt was made to explain if proppant embedment occurred for each sample.

As previously noted, the fracture conductivity reduces because the fines created from crushed proppant can lead to fines migration and embedment (Cooke, 1977). When embedment occurs, the pore channels become blocked and the flow from the reservoir decreases. The calculated changes in fracture surface volumes were used to explain how the fracture surfaces changed during a fracture job and, most importantly, how fracture conductivity was negatively impacted. It is important to note the experiments performed did not account for flow traveling from the reservoir into the fracture perpendicularly (i.e. flow that would be perpendicular to the flow of nitrogen in the experiments ran).

2.3.3 Proppant Placement and Epoxy Coating

After surface scans were taken for all samples, the appropriate proppant type was spread evenly on the respective sample's bottom fracture surface, as indicated in **Figure 13**.

(a)   (b)
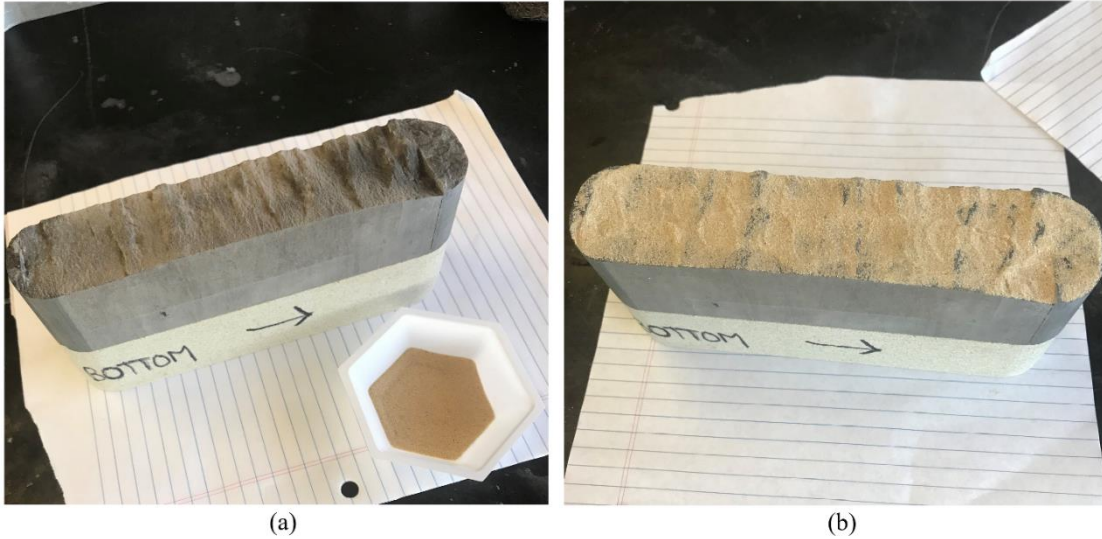
This process was done over a piece of paper. To ensure all samples were consistently

Figure 13. (a) The weighed proppant and the bottom of Sample No. 2; (b) the proppant spread evenly on the fracture surface.

loaded, the stray grains that fell onto the paper during the spreading process were poured back onto fracture surface.

After all proppant grains were distributed on the fracture, an epoxy resin was fashioned onto the outer surfaces of the core and Berea sandstone spacers. When the sample was inside the Modified API cell, the epoxy resin prevented pressure leak off and stabilized the sample. The following steps explain how the resin was cured onto the samples. While performing these steps, the samples were handled with extreme care (i.e. not tipped sideways or jostled) in order to prevent the proppant grains from shifting inside the fracture.

1. The top fracture surface is placed evenly and gently onto the bottom fracture surface
   (**Figure 14a**).

<div align="center">(a)   (b)</div>
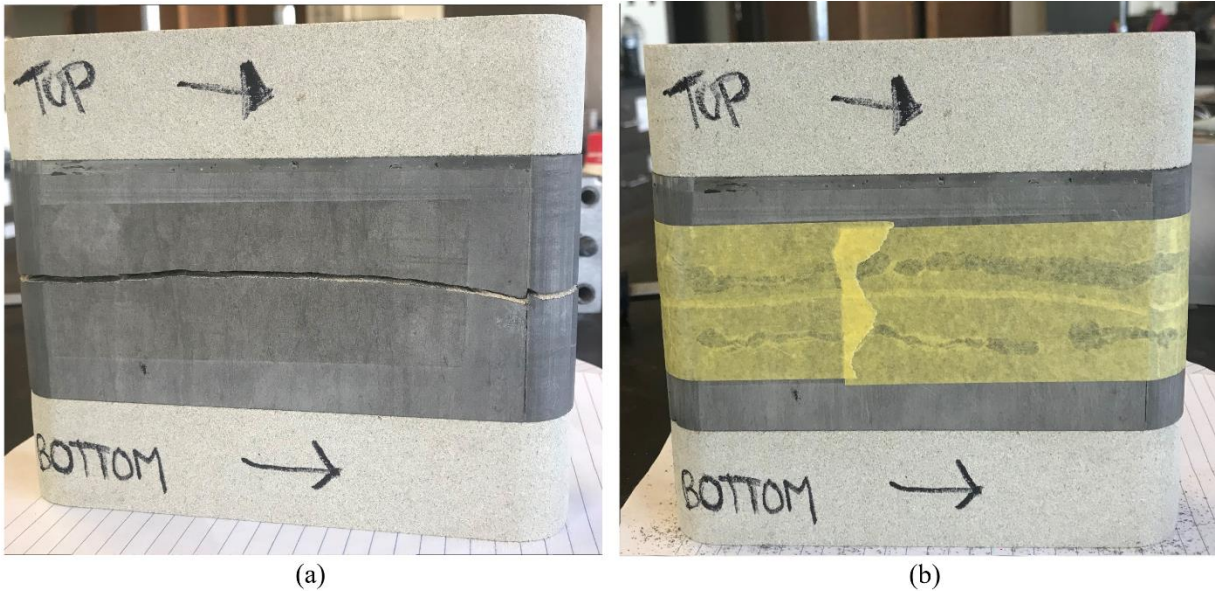
Figure 14. (a) The top fracture surface evenly placed on the bottom surface with proppant distributed between the two surfaces; (b) Tightly wrapped Painter's tape glued and smoothed with steel wool around the fracture.

2. To prevent the resin from leaking into the fracture, painter's tape is glued tightly around
   the fracture (**Figure 14b**).

3. Steel wool is used to smooth down the tape and remove any air bubbles or tape creases. If
   the tape is not completely smooth around the propped fracture, the epoxy resin will settle
   unevenly and air pockets will form. If air pockets form, there will be pressure leak off
   and nitrogen channeling around the cell during the fracture conductivity experiment.

4. Inside a laboratory fume hood, a primer is generously painted onto the sample (**Figure 15**). This primer binds the epoxy resin to the rock and tape surfaces. After 15 minutes, another layer of primer is applied. The sample is coated a total of three times with a dry time of 15 minutes per layer.

Figure 15. The primer and sample inside a laboratory fume hood.

5. Once the surfaces of the mold that face the sample are cleaned with acetone and all debris are removed, a mold release is sprayed onto these surfaces (**Figure 16**). With a 5-minute dry time between each layer, three layers are applied. The mold release spray prevents the epoxy from adhering to the mold's metal surface and tearing away from the sample.

Figure 16. The mold with the chemicals used to prepare it for the sample and epoxy resin.

6. High pressure vacuum grease is applied to the surfaces of the mold where metal touches metal when the mold is assembled. This step helps prevent the epoxy resin from leaking through the mold's seams.

7. The three components of the mold shown in **Figure 16** are tightly screwed together. After the third layer of primer is finished drying for 15 minutes, the sample is gently placed inside the mold (**Figure 17**).

Figure 17. The mold with the sample centered inside with the application syringe and epoxy resin mix.

8. The two components of the epoxy resin are mixed using a 50:50 ratio. A syringe is used to slowly pour the resin mix into the void space between the mold and the sample. A slow pour allows the epoxy to settle and prevent the formation of trapped air bubbles.

9. Once the epoxy resin reaches just below the top of the mold, the mold is placed in the oven to cure for 2 hours at a temperature of 125° (number 4 dial setting on the oven).

10. After 2 hours, the mold is removed from the oven and the sample is carefully removed from the mold (**Figure 18**).

Figure 18. The sample in the mold after curing in the oven for 2 hours.

11. Steps 1 through 11 are repeated for the top half of the sample. Spacers are used to support the mold brackets around the sample (**Figure 19**). The bottom plate is no longer needed

and can be set aside. The mixed epoxy resin is again poured to completely encase the sample.

(a)   (b)
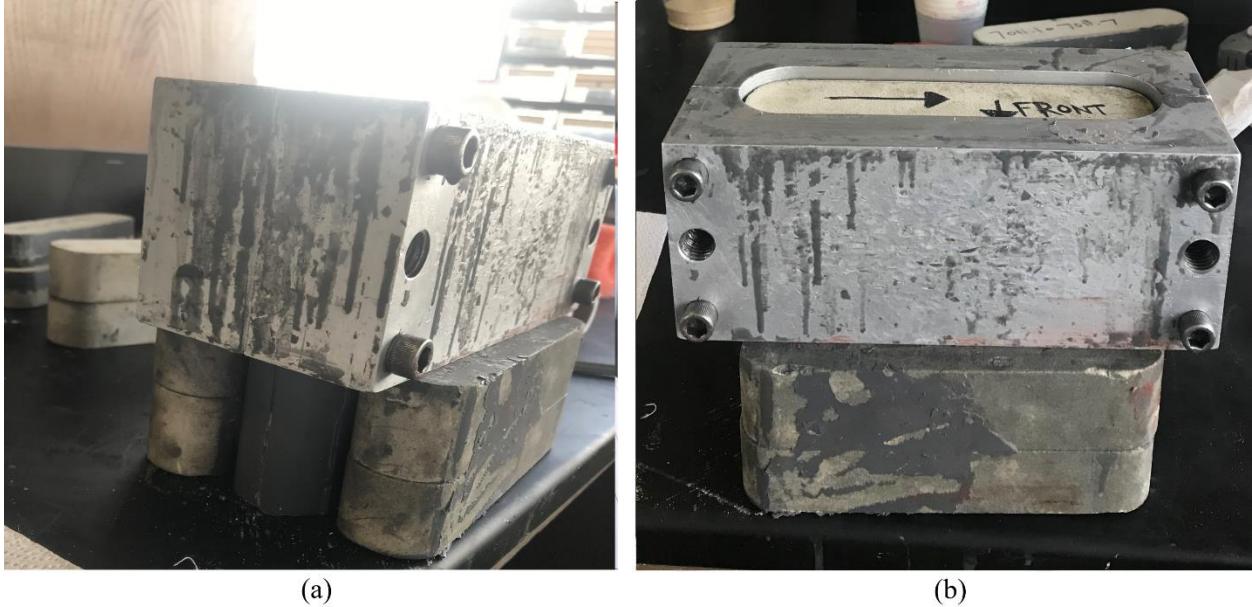
Figure 19. The mold encasing the top half of the sample before the epoxy was poured: (a) side view; (b) top view.

For some samples, the epoxy did not settle perfectly and small air bubbles formed leaving gaps and exposing the sample. High temperature red RTV silicone sealant was injected into these gaps and smoothed to evenly align with the epoxy surface. This sealant required a few hours of dry time depending on the amount used.

2.4 Propped Fracture Conductivity Experimental Methodology

This section explains the experimental design, set up and procedure for executing the fracture conductivity experiments. Detailed explanations of the equipment used are provided, as well as, the derivation of the equations used to quantify fracture conductivity.

2.4.1   Conductivity Equation Derivation

The Darcy equation (**Eq. 3**) and Forchheimer equation (**Eq. 4**) were used to derive the equation for calculating fracture conductivity in the laboratory setting.

$$-\frac{dp}{dL} = \frac{\mu v}{k_f} \tag{3}$$

$$-\frac{dp}{dL} = \frac{\mu v}{k_f} + \beta \rho_f v^2 \tag{4}$$

Where $-\frac{dp}{dL}$ is the pressure drop over a unit length, v is fluid velocity, μ is fluid viscosity

(cP), k_f is fracture permeability (md), β is an inertial factor, and ρ_f is fluid density (kg/m^3).

Awoleke (2013) concluded that for nitrogen flow rates pumped through the fracture higher

than 0.9 L/min, the Forchheimer equation should be applied. Similar to Awoleke, Zhang (2014)

concluded for nitrogen flow rates above 0.8 L/min, the Forcheimer equation should be applied.

In contrast, McGinley (2015) concluded Darcy flow can be applied for flow rates below 2 L/min.

Winner (2018) supported McGinley's conclusion and used the Darcy Law derivation to

quantify fracture conductivity for his Meramec core. A low proppant concentration of 0.2 lbm/ft^2

was used for all samples and the fracture conductivity equation derived from the Darcy equation

was used when flow rates that did not exceed 2 L/min.

To begin the derivation, **Eq. 3** was multiplied by the density of the fluid pumped through

the fracture, ρ_f. This was the first step in removing velocity, an unknown, from the equation.

$$-\frac{dp}{dL}\rho_f = \frac{\mu v}{kf}\rho_f \tag{5}$$

With nitrogen being the fluid pumped through the system, the real gas law, or **Eq. 6**,

could be applied.

$$\rho_f = \frac{pM_g}{ZRT} \tag{6}$$

Where p is pressure, M_g is molecular weight (0.0280134 kg/mol), Z is the gas

compressibility factor (1), R is the universal gas constant (8.3144 J/molK), and T is temperature

(293.15 K). Next, **Eq. 7** was used to eliminate the unknown values in **Eq. 5** and to introduce

values that could be measured in the lab. Both in the lab and field settings, pressures and flow

rates can be more realistically quantified, as opposed to permeabilities.

$$\rho_f = \frac{\dot{M}}{Av} \tag{7}$$

Where $\dot{M}$ is mass flow rate and A is flow rate. **Eq. 5**, **Eq. 6**, and **Eq. 7** were combined to

form **Eq. 8**. **Eq. 8** was then integrated into **Eq. 9.**

$$-\frac{pM_g}{ZRT}dp = \frac{\mu\dot{M}}{k_fA}dL \tag{8}$$

$$\frac{(P_1{}^2-P_2{}^2)}{2}\frac{M_g}{ZRT} = \frac{\mu\dot{M}}{k_fA}L \tag{9}$$

Where L is the length of the flow path, P_1 is the upstream pressure, and P_2 is the

downstream pressure inside the fracture. In the propped fracture, there are two pressures that

should be consider when determining P_1 and P_2 : cell pressure and differential pressure. Both were

measurable through the pressure ports on the front of the Modified API cell (**Figure 20**).
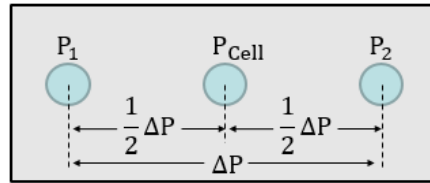
Figure 20. A schematic of the pressures measured from the port holes in the front of the
Modified API cell.

As shown in **Figure 20**, the cell pressure, P_{Cell}, was measured from the center pressure

port. The pressure drop, or differential pressure, ΔP, throughout the fracture was measured using

the first and last pressure ports. These two ports were an equal distance away from the center

port. Therefore, P_1 and P_2 in **Eq. 9** and **Figure 20** can be computed with **Eq. 10** and **Eq. 11**, respectively.

$$P_1 = P_{cell} + 0.5\Delta P \tag{10}$$

$$P_2 = P_{cell} - 0.5\Delta P \tag{11}$$

The remaining known and unknown parameters needed to calculate area (**Eq. 12**) and the mass flow rate (**Eq. 13**) were substituted into **Eq. 9** to create **Eq. 14**.

$$A = w_f h_f \tag{12}$$

$$\dot{M} = q\rho_f \tag{13}$$

Where w_f is fracture width, h_f is fracture height, and q is volumetric flow rate.

$$\frac{[(P_{cell}+0.5\Delta P)^2 - (P_{cell}-0.5\Delta P)^2]}{2L} \frac{M_g}{ZRT} = \frac{\mu q\rho_f}{h_f} \frac{1}{w_f k_f} \tag{14}$$

As previously stated, fracture conductivity, C_f, is the product of permeability and fracture width. Both values are unknown.

$$C_f = k_f w_f \tag{15}$$

This definition of fracture conductivity was inserted to simplify **Eq. 14** and create **Eq. 16**.

$$\frac{[(P_{cell}+0.5\Delta P)^2 - (P_{cell}-0.5\Delta P)^2]}{2L} \frac{M_g}{ZRT} = \frac{\mu q\rho_f}{h_f} \frac{1}{C_f} \tag{16}$$

The sections that proceed will explain how the pressures in **Eq. 16** were determined. h_f and L are the measurable width and the length of the sample, respectively. The remaining unknown is C_f.

To determine fracture conductivity, $\dfrac{[(P_{cell}+0.5\Delta P)^2 - (P_{cell}-0.5\Delta P)^2]}{2L}\dfrac{M_g}{ZRT}$ versus $\dfrac{\mu q \rho_f}{h_f}$ was

simplified and plotted. From this relationship depicted in **Figure 21**, the inverse of the slope

from this plot is fracture conductivity.
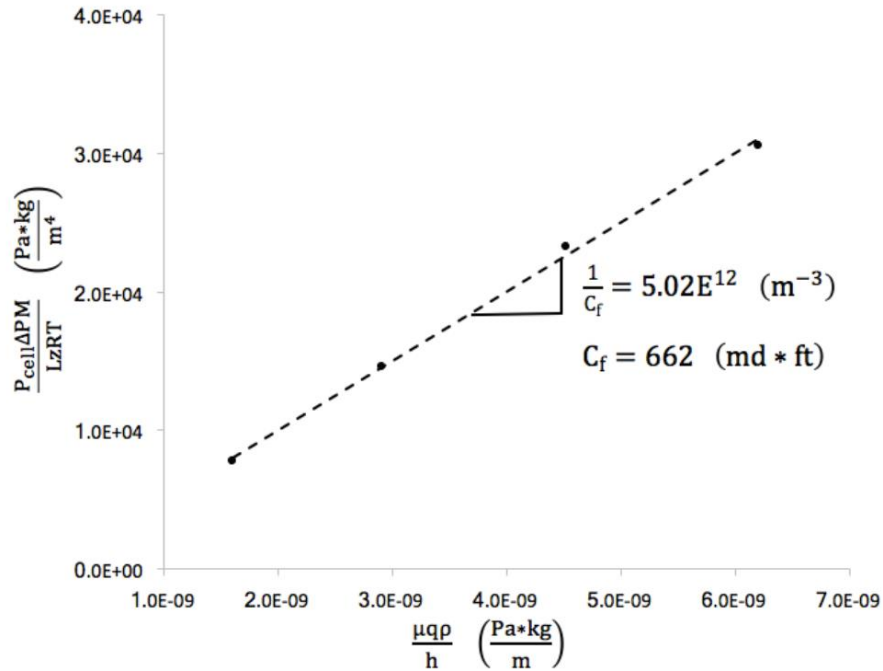
Figure 21. Using the experimental results to determine fracture conductivity (modified from Wylie, 2018).

.

For flow rates above 2 L/min, the Forchheimer method derived by Zhang (2014) can be

used. He introduced plotting $\dfrac{P_{cell}M_g\Delta P h_f}{ZRTL\mu q \rho_f}$ versus $\dfrac{q\rho_f}{h_f \mu}$. The inverse of the y-intercept from this

plot yields fracture conductivity. Again, this method was not employed for this project because

the flowrates did not exceed 2 mL/min for the 0.2 lbm/ft^2 proppant concentrations.

2.4.2 Experimental Design

The experimental system utilized to quantify fracture conductivity included the following

primary components:

(1) Modified API fracture conductivity cell

(2) GCTS hydraulic load frame

(3) Nitrogen gas reservoir contained in a pressurized dry nitrogen aluminum cylinder

(4) Cell and differential pressure transducers

(5) Gas flowmeters

(6) Backpressure regulator

(7) GTCS control system connected to a PC containing a data acquisition software

Before the detailed explanations are provided for each of these components, a schematic of

the experimental system is below to clarify how they are related to the experiment as a whole.
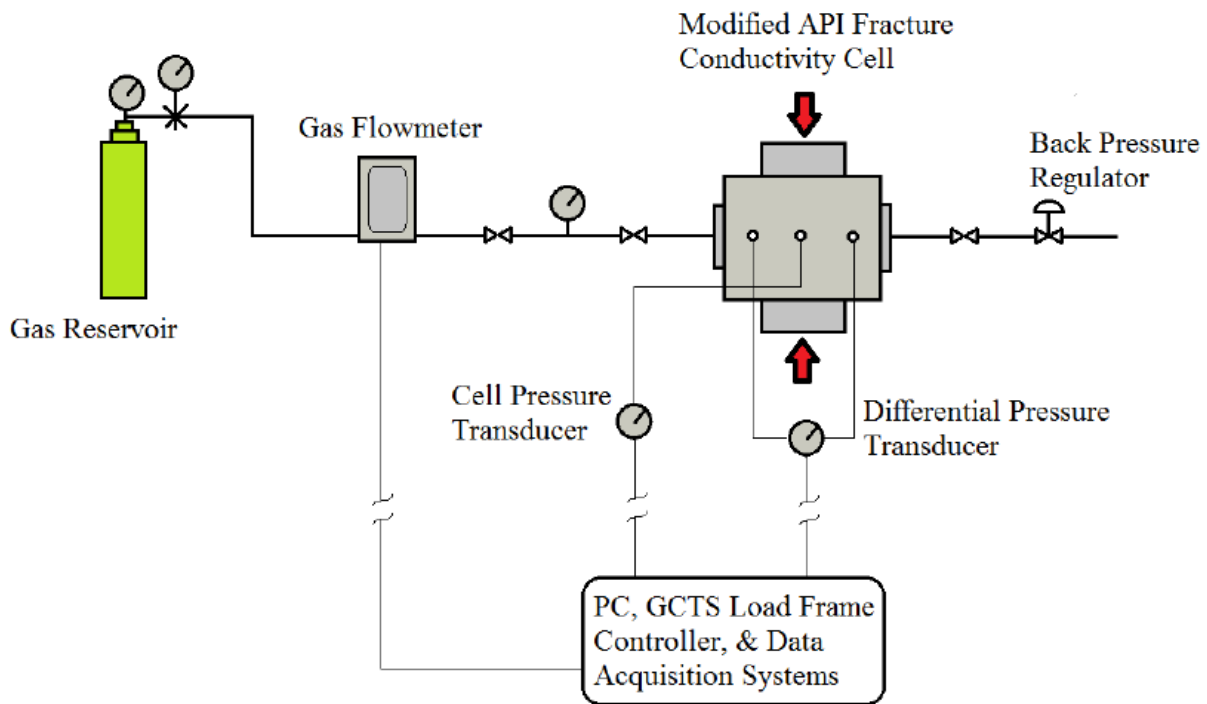
Figure 22. The experimental schematic for quantifying fracture conductivity (modified from Guerra, 2019).

The propped and then epoxied samples were carefully placed inside the cell and a load was

applied to the top piston inserted in the cell. The samples were loaded to 1,000 psi, 2,000 psi,

3,000 psi, and 4,000 psi closure stresses. At each closure stress, nitrogen gas was pumped

through ¼ in. flow lines from the aluminum tank into the Modified API fracture conductivity cell

and through the propped fracture, while the gas flowmeter outputted the flowrate.

The transducers measured the pressure changes inside the cell. The GCTS CATS software

on the PC recorded all measurements acquired throughout the experiment. The backpressure

regulator controlled the flow exiting the cell and helped regulate the pressure inside the cell. The

following **Figure 23** illustrates the real experimental setup used the laboratory. A more detailed

test procedure is provided in Section 2.4.4.
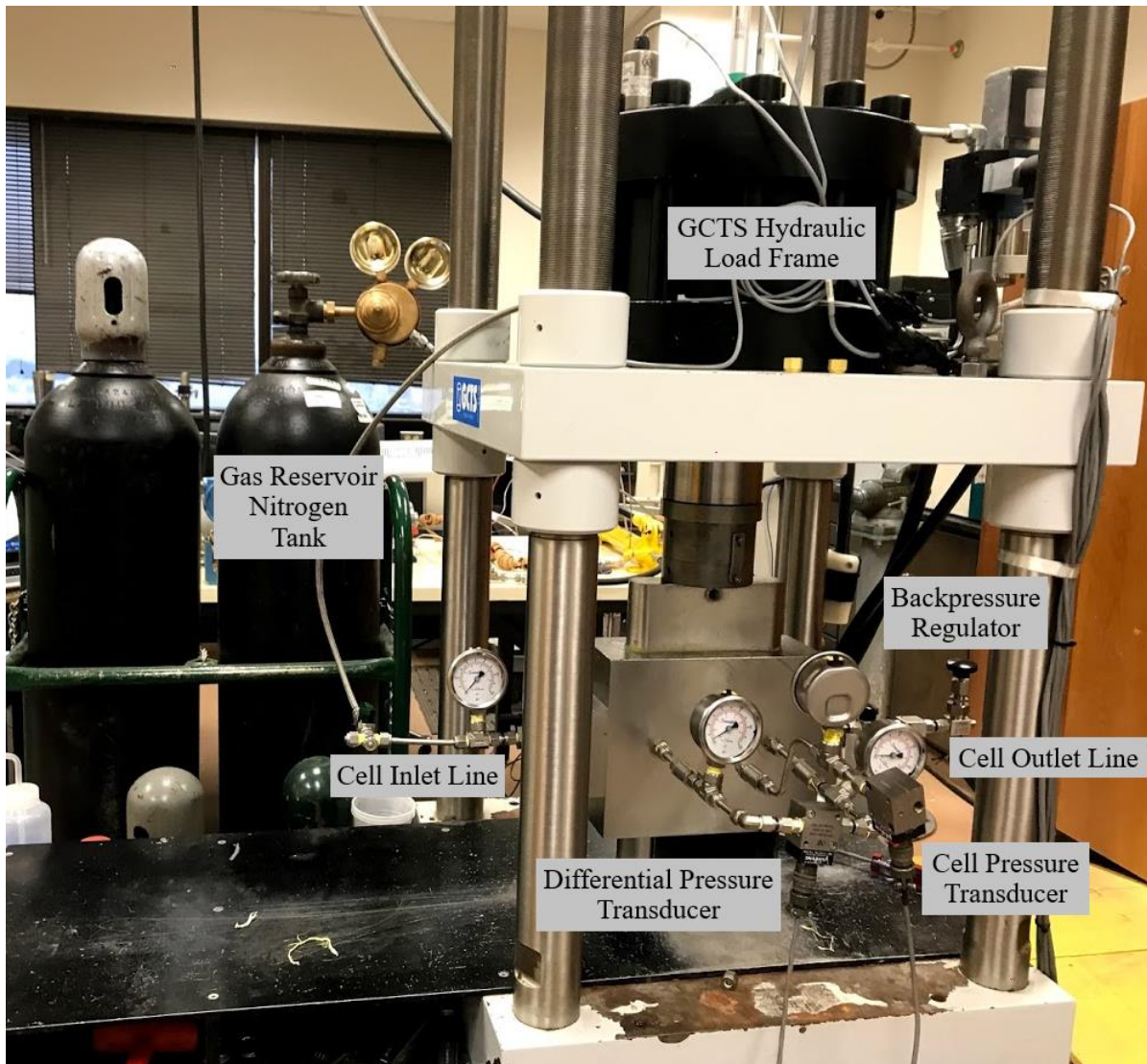
Figure 23. The experimental set up in the laboratory.

2.4.3   Experimental Equipment

The experimental set-up used for this study has been implemented and modified over the years for various fracture conductivity studies. For example, the studies done by Kamenov (2013), Zhang (2014), and Guerra (2019). Each component notated in **Figure 23** played an important role during the conductivity experiments.

The GCTS load frame used was a GCTS FRM4-1000-50s loading system with a loading capacity of 208,000 lb_f and a maximum loading rate of 1,215 lb_f/min. The hydraulic pump driving the load frame is operated by a control box linked to a computer containing an acquisition system that collects the data. The software downloaded on the PC outputs: the closure stress being applied to the sample, the axial displacement of the load piston, the pressure inside the cell, and the differential pressure inside the fracture. These outputs were used to calculate the fracture conductivity inside the Modified API cell.

This stainless steel cell securely holds the prepared sample in place during testing (**Figure 24c**). The three ports located on the front of the cell are where the cell and differential pressure transducer lines are secured. Once portions of the epoxy are cut away to expose the fracture, the propped fracture should be aligned with these ports. The outer cell dimensions are 10 in. (length) by 4 in. (width) by 8 in. (height). The inner cavity's dimensions, where the sample is carefully inserted, are 7 in. (length) by 1 in. (width) by 8 in. (height), while accounting for a circular end radius of 0.8785 in.

Figure 24. The key components used to quantify fracture conductivity: (a) an aluminum cylinder containing industrial grade dry nitrogen connected to a regulator valve; (b) an Aalborg flowmeter connected the nitrogen gas flow line; (c) components to the test apparatus: Modified API fracture conductivity cell, top and bottom pistons, and the cell's end caps (modified from Guerra, 2019); (d) Validyne pressure transducers connected to flow lines and pressure gages (modified from Guerra, 2019).

The dimensions for the pistons next to the Modified API cell in **Figure 24c** are 7 in. (length) by 1 in. (width) by 3 in. (height). Securing the sample correctly inside the cell with these pistons was key because the pistons distribute the load from the hydraulic load frame onto the sample. An evenly distributed load onto the sample was desired. Therefore, the load pistons were aligned with the sample in the cell and inserted above and below the cell into the cell cavity.

37

Section 2.4.4 provides more detail on inserting the sample and constructing the conductivity apparatus.

Each piston has an inner tubular conduit connecting the base of the piston to the outer port located at the top of the piston. This conduit allows for the installation of leak-off lines, if needed. For all experiments, the bottom ports were sealed with steel plugs. To further prevent pressure and nitrogen leak off from the cell, the tops of the pistons, as well as the cell endcaps, were equipped with a Viton polypack seal o-ring. The o-ring ensured a tight connection between the piston and the cell cavity wall. Once the sample was loaded to the initial closure stress of 1000 psi, the cell endcaps were inserted and screwed into the sides of the cell. They were then connected to the nitrogen inlet and outlet lines and allowed for the nitrogen to be pumped through the propped fracture.

Aalborg XFM17 Digital Mass Flow Meters were installed to measure the mass flow rate of the nitrogen traveling from the gas reservoir to Modified API cell (**Figures 24a and 24b**). Two flow meters were initially selected for the experiment with capacities of 1,000 mL/min and 10,000 mL/min. These flow meters were calibrated by the manufacturer for nitrogen flow. They both had a measurement accuracy of ± 1% of the full scale flow rate. For example, for a set flow rate of 700 mL/min, the 1000 mL/min capacity flow meter had a measurement error of ± 10 mL/min and the 10,000 mL/min capacity flow meter had a measurement error of ± 100 mL/min (Guerra, 2019).

After the first experiment, it was apparent the flow meter with a higher capacity was more applicable because flowrates of around 1000 – 1500 mL/min yielded more recordable differential pressure measurements. Differential pressure and cell pressure measurements were recorded using Validyne pressure transducers (**Figure 24d**) with exchangeable internal sensor

diaphragms. The Validyne Model DP15 50N1S4A with a 3-50 diaphragm and pressure threshold of ±125 psi was used to measure cell pressure. The Validyne Model DP15-32 with a 3-32F diaphragm and pressure threshold of ± 3.5 psi was used to measure the differential pressure in the propped fracture.

Once the cell was pressurized to a cell pressure of 30 psi, the cell and differential pressures could be increased or decreased by twisting the backpressure regulator valve connected to the cell outlet flow line. A Swagelok needle valve was the backpressure regulating valve installed for the experiments. By twisting the needle valve, the flow of nitrogen out of the cell could be carefully manipulated.

2.4.4   Propped Fracture Conductivity Procedures

The following steps were implemented in the laboratory to measure fracture conductivity for the prepared propped shale samples. To ensure the proppant remained undisturbed, the steps involving the sample were done very gently. Before each experiment, the differential and cell pressure transducers were calibrated. The propped fracture conductivity test procedures are as follows:

1) Log into the laboratory PC.

2) Turn on the GCTS control box.

3) Turn on the flowmeter by plugging the power cord into outlet.

4) Check the nitrogen flow regulator valve attached to the nitrogen tank is closed. Open the main valve to allow the tank to pressurize. (**Figure 25**).

Figure 25. The gages and valves connected the nitrogen tank.

5) Cut five windows out of the epoxy to expose the fracture: three evenly spaced in the front and one on each side of the sample. These windows need to align with the three ports located on the front and the inlet and outlets on the sides of the Modified API cell. See **Figure 26** for the measured locations of each window.
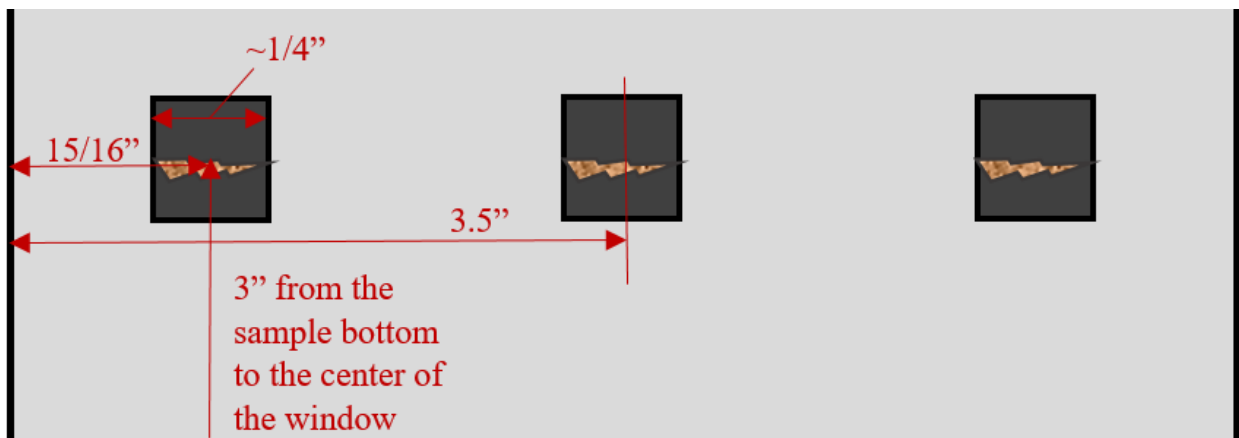
Figure 26. The measurements used to cut away the epoxy and expose the propped fracture to the pressure transducer ports on the front of the cell.

When cutting the two windows on the sides of the sample, measure 3 in. from the bottom of the sample to the center of the window. The center of this window should be aligned with the center of the side of the sample (**Figure 26**).

6) Tightly wrap one layer of sealant tape around the sample in six locations to help prevent pressure leak off and nitrogen channeling around the sample (**Figure 27a**).
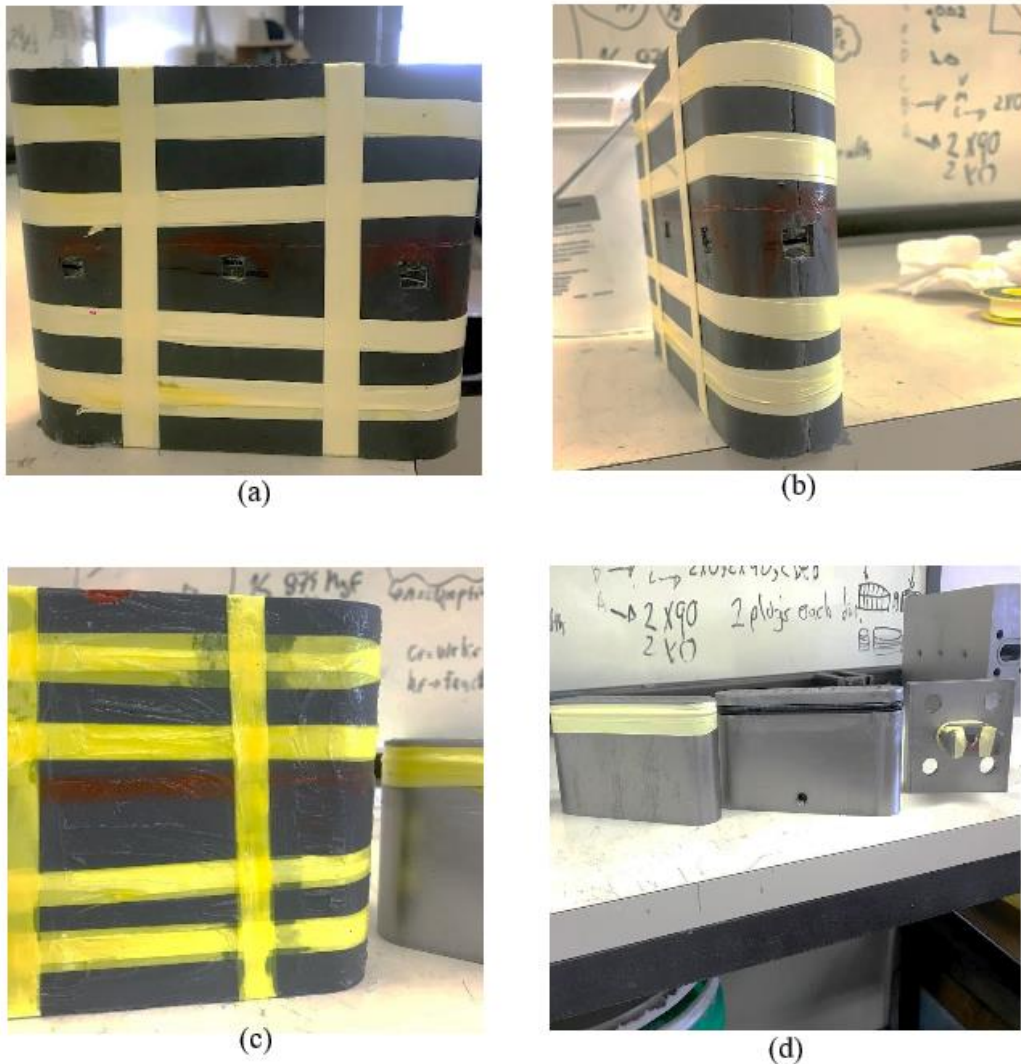
Figure 27. The final sample preparation required before running the fracture conductivity test: (a) front of the sample tightly wrapped with sealant tape and the three windows cut out; (b) side of the sample with the side window exposing the fracture; (c) a thin layer of vacuum grease applied to the sample and the tape wrapped around the piston o-ring; (d) sealant tape applied to one of the pistons (left), tape applied to the end cap (right), and the bare piston before tape was applied (center).

7) Tightly wrap three layers of sealant tape around both rubber o-rings located at the tops of the pistons (**Figure 27d**).

8) Place screens in both endcaps to prevent proppant migration from the fracture and into the flow lines. A taped endcap is shown in **Figure 27d.**

9) Apply a thin layer of clear high pressure vacuum grease onto the epoxy surface (**Figure 27c**). Do not put any grease below the windows. There should be no grease in or close to the fracture after it is inserted into the Modified API cell. Also, apply a thin layer onto the tape wrapped around the pistons.

10) On the black metal surface to the left of the GCTS load frame, place the bottom piston inside the black bracket with the port hole facing forward. The port hole should align with the bracket gap.

11) Determine the top of the Modified API cell (the A and B engraved on the sides of the cell should be orientated in the up-right direction) and align the bottom of the cell cavity with the top of the piston. The three pressure ports on the front should be facing forward. Firmly press the cell until is rests evenly on the bottom bracket.

12) Carefully align the front of the sample above the cell cavity and slowly push the sample down into the cavity (in the past, other graduate students used a hydraulic press to insert the sample, if needed, as shown in **Figure 28a**).
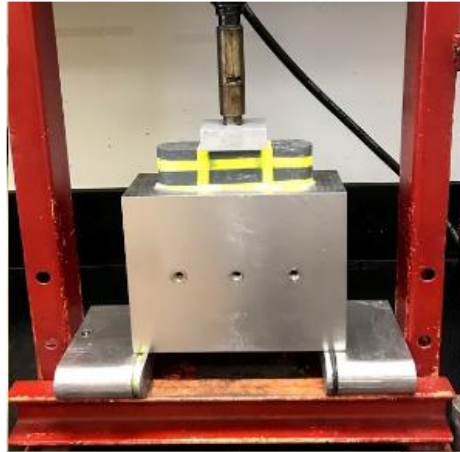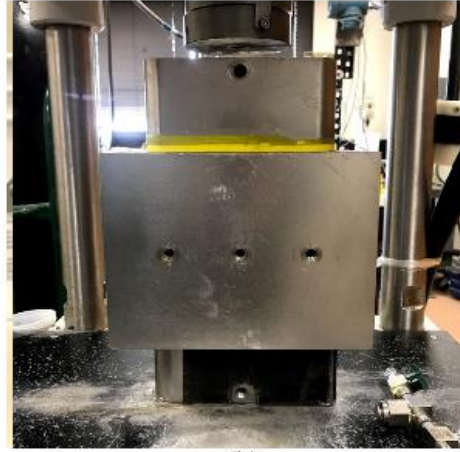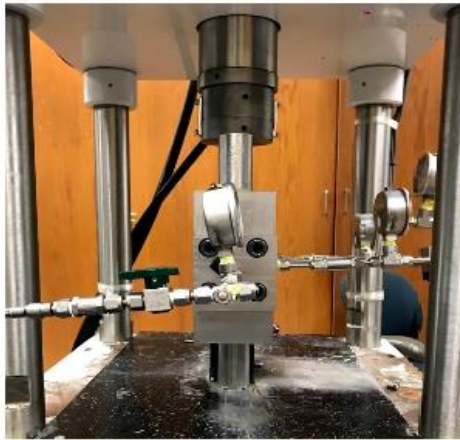
Figure 28. Assembling the experimental setup: (a) a hydraulic press can be used to insert the sample into the cell, if needed; (b) under the load press, the bottom piston and bracket are supporting the cell and top piston; (c) left side view of the set up (inlet); (d) right side view of the set up (outlet and backpressure regulator).

13) Under the GCTS load frame, place the top piston with the tape side on top of the sample in the cell (**Figure 28b**).

14) Center the top piston under the load press by gently moving the bottom piston and bracket. If the piston is not centered in both the parallel and perpendicular directions, the top piston will jam in the cavity.

15) Insert and tighten the respective plugs into the top and bottom piston ports.

43

16) Open the GCTS CATS software.

17) In the "System" drop down window, select "Configuration" and select "GCTS_1646".

18) In the "Views" drop down window, select "Load Screen Layout" and select the desired screen layout (**Figure 29**).The load screen layout should have digital views for cell pressure, differential pressure, axial displacement, and axial load.
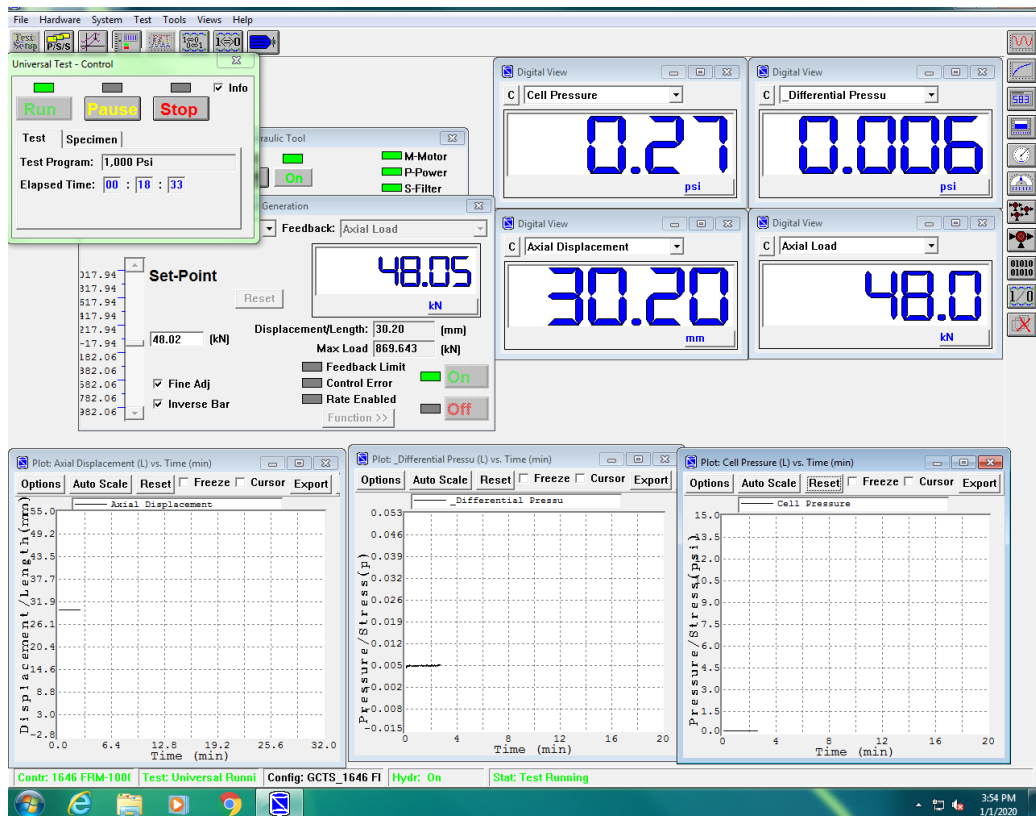
Figure 29. The load screen layout for a closure stress of 1000 psi.

19) Turn the pump on by selecting the pump icon and clicking "On".

20) In the "System" drop down menu, select "Configuration" and "Synchronize".

21) Load the sample to a closure stress of 1,000 psi by following these steps:

    a.   Click the Projects icon.

    b.   Select the project.

    c.   Click the right arrow.

d. Enter the sample information.

e. Click ok.

f. Click the right arrow.

g. Click "New" and enter the "1000 psi" for the ID.

h. Click the right arrow.

i. Select "1000 psi".

j. Click "Execute"

22) Click "Run". The system will begin lowering the load press.

23) Monitor the press and top piston for shifting.

24) Insert the screens into the pressure ports on the front of the cell to ensure proppant doesn't migrate into the pressure transducer lines.

25) Once the sample is loaded to a closure stress of 1,000 psi or 48 kN, insert and tightly screw the endcaps into the correct sides of the cell. The endcap engraved with an "A" should be inserted into the side of the cell also engraved with an "A".

26) Tightly screw the differential and cell pressure lines to the front of the cell.

27) The differential and cell pressure digital readings should be close to zero. To zero readings, select "Tools" and select "Inputs Offsets".

28) Tightly attach the inlet and outlet flow lines to the respective cell endcaps.

29) Tightly close the backpressure valve.

30) Pressurize the cell to a cell pressure of 30 psi (digital view) by very slowly twisting the nitrogen regulator valve. To prevent blowing out the proppant, the nitrogen flowrate should not exceed 100 mL/min or 0.1 L/min when pressurizing the cell.

31) At 30 psi, stop twisting the valve. The flowrate will drop. Record the leak off flowrate.

32) Allow flow through the cell by slowly opening the backpressure valve until a desired flowrate or differential pressure is reached.

    a. The flow should not exceed 2 L/min. The differential pressure should not exceed 3 psi or the membrane inside the transducer will be damaged.

    b. A differential pressure of 0.100 psi was desired for the first readings during the experiments performed for this project.

    c. The same starting flow rate for each load stage should be used.

33) Record the flowrate, differential pressure, cell pressure, and axial displacement.

34) Take 4 measurements at each closure stress. Establish target pressure drops for an average fracture conductivity measurement at each closure stress. Divide the first differential pressure by 4 and that value will be the change in pressure between measurements.

35) Slowly twist the backpressure regulator to the right until the differential pressure reaches the next target pressure.

36) Record the flowrate, differential pressure, cell pressure, and axial displacement.

37) Repeat Steps 32 and 33 until 4 readings are recorded.

38) Twist the nitrogen regulator valve to the left and close the system off to nitrogen flow from the tank.

39) In the GCTS software, click "Stop".

40) Enter "2000 psi" for the new specimen ID.

41) Select "2000psi".

42) Click "Execute" and click "Run". The system will now load the sample to a closure stress of 2000 psi.

43) When the cell pressure reaches ~10 psi, open the backpressure valve while watching the differential pressures and flowrates.

44) Once the sample is loaded to a closure stress of 2,000 psi and the cell pressure is ~0 psi, close the backpressure valve.

45) Repeat Steps 29 through 36.

46) Repeat Steps 37 through 39, but for a closure stress of 3,000 psi.

These steps should be followed until four measurements are taken at closure stresses 1,000 psi, 2,000 psi, 3,000 psi, and 4,000 psi. Using the flowrates, differential pressures, axial displacements, and cell pressures recorded, an average fracture conductivity valve can be calculated at each closure stress.

47) After the final reading is recorded at a closure stress of 4000 psi, close the main valve on the nitrogen tank. The backpressure valve may need to be opened a little more if the nitrogen tank pressure is not noticeably dropping. Be cautious of the differential pressures when twisting the backpressure valve.

48) In the GCTS software, load the sample to 1,000 psi again.

49) Once the nitrogen tank gage reads 0 psi, twist the nitrogen regulator valve to the left and close off the system to the nitrogen tank.

50) When the cell pressure reaches ~10 psi, open the backpressure valve completely.

51) When the cell pressure and differential pressure reaches ~0 psi, remove the inlet and outlet lines, pressure transducer lines and endcaps.

52) In the GCTS software, click "Stop".

53) Enter "unload" for the new specimen ID.

54) Select the unload option.

55) Once the axial displacement is ~0 mm, shut the pump off.

56) Click "File" and select "Shut Down Controller".

57) Turn off the controller.

58) Remove and separate the cell and pistons. The hydraulic press can be used to gently push out the bottom piston and sample.

2.5 Key Design Considerations and Experimental Challenges

With the amount of steps required to execute the fracture conductivity experiment, the chance of user error was high. The following were considered while designing and working through the procedures:

1. The Modified API cell should not lose pressure and the nitrogen should not channel around the sample. Nitrogen flow should only occur through the propped fracture when pumped into the cell. Pressure leakage leads to inconsistent readings and skewed fracture conductivity measurements. To prevent pressure leakage, the sample needs to be evenly coated with epoxy and all flow line connections should be securely fastened. High pressure vacuum grease can be used to help seal unexpected leaks.

2. The uniform proppant distribution inside the fracture should be maintained during the sample preparation and experimental set-up. If the sample is jostled or tipped, the proppant grains could shift and impact proppant behavior (i.e. proppant channeling). In order to properly compare the results from the experiments performed with different samples, the proppant distribution and loading should be consistent amongst the samples.

3. When pressurizing the Modified API cell, the nitrogen flow rate should be closely monitored, especially when working with smaller proppant grains. Flow rates close to 100 mL/min should be used to prevent proppant from being blown out.

3. RESULTS AND DISCUSSION

3.1 Introduction

In this section, the results from the compared surface profilometer scans taken before and after the samples were tested are provided. The surface volume changes yielded from the MATLAB codes are tabulated and discussed. The results from the fracture conductivity tests are also provided with detailed discussion.

3.2 Fracture Surface Profilometer Scans

As previously explained in Section 2.3.2, a laser profilometer was used to scan the fracture surfaces. To generate 3-dimensional profiles of the surfaces, the output (x,y,z) measurements were loaded into MATLAB. MATLAB codes were used to determine the surface volume changes after the conductivity tests and then discuss if proppant embedment occurred.

3.2.1 Surface Volume Changes and Proppant Embedment Estimation

Surface scans were taken of each sample before they were prepared for the fracture conductivity test and after the test was performed. The MATLAB code compared the data collected and calculated the volumetric change in surface dimensions for both the top and bottom fracture surfaces. The results are listed in **Table 3**.

Table 3. The volumetric changes of the fracture surfaces before and after the conductivity experiments.

Sample Number: Core Type	Proppant Type	Change in Volume (in^3)	
		Bottom Surface	Top Surface
Sample No. 1: Meramec	Provided	0.013	0.026
Sample No. 2: Meramec	Provided	-0.003	0.015
Sample No. 3: Meramec	Created	0.036	0.108
Sample No. 4: Meramec	Created	0.084	0.047
Sample No. 5: Eagle Ford	Provided	0.030	0.091
Sample No. 6: Eagle Ford	Provided	0.059	0.099
Sample No. 7: Eagle Ford	Created	0.126	0.111
Sample No. 8: Eagle Ford	Created	0.256	0.106

It is important to note this method of analysis captured only surface volume changes. The volume of proppant that may have embedded below the fracture surface was not considered in the volume calculations. Only the changes in fracture surface heights were estimated. However, it is reasonable to assume the surfaces with larger surface volume increase experienced the highest proppant embedment. With this being said, the samples propped with the created proppant exhibited a larger increase in the bottom and top surface volumes than samples propped with the provided proppant. This may mean more fines were produced by the created proppant due to proppant crushing.

The negative measured volume change for Sample No. 2's bottom surface was unexpected and very different from the other samples. Due to this disparity, further analysis of all the surfaces was done. It was found from the images taken of the surfaces after the experiments, that Sample No. 2 experienced noticeable surface fracturing, as shown in **Figure 30**. It was concluded pieces of shale broke away from the sample surface and skewed the surface change results, deeming them unreliable.

Figure 30. Indicated with the red arrow, the fracture that formed in the fracture surface after Sample No. 2 was tested.

Continuing the discussion on **Table 3,** Eagle Ford samples No. 6 – 8 yielded higher volume changes than the Meramec samples. This was an expected result because in some locations on the Eagle Ford fracture surfaces, there was noticeable proppant embedment. With the naked eye

in the laboratory, very fine proppant grains embedded in the shale surface could be seen. The disparity between the embedment that occurred for the Eagle Ford samples versus the Meramec samples can be attributed to the differences between the two shales' mineralogy.

Guerra et al. (2017) used XRD to estimate the average mineral composition for Eagle Ford samples also pulled from the Terrell County, Texas outcrop. All samples examined were primarily comprised of calcite (55-95%). Winner (2018) used XRD to examine Meramec core that was pulled from the same downhole conditions as the samples tested in this thesis. He found the Meramec core was primarily composed of quartz (36-68%). This distinction impacts proppant embedment because quartz is much harder than calcite. Quartz reaches 7 on the Mohs scale of mineral hardness, whereas calcite's hardness is 3 (Zinni, 2013). When the samples were being exposed to the high closure stresses, the proppant proved to be more likely to embed into the softer Eagle Ford sample.

3.3 Propped Fracture Conductivity Test Results and Discussion

This section provides the calculated fracture conductivity values for the propped Meramec and Eagle Ford shale cores, as well as images of the proppant distribution after the experiments. All samples were loaded to a maximum closure stress of 4,000 psi. Initially, for all eight samples, a proppant concentration of 0.2 ft/lbm^2 was used.

However, after reviewing the results, the four Eagle Ford core samples were prepared again with a 0.1 ft/lbm^2 concentration of the provided and created proppants. These additional experiments were ran to discover if the same results could be achieved with a lower proppant loading. The goal was to also verify the validity of the results from the first batch of experiments. The results from these additional tests are detailed in Section 3.3.4.

3.3.1 Meramec Core

Four samples made with Meramec downhole core were tested; two with a provided 100-mesh proppant and two with a proppant made from the grains collected by the No. 120 sieve. The fracture conductivity values yielded, using **Eq. 16,** at each closure stress are plotted in **Figure 31.**
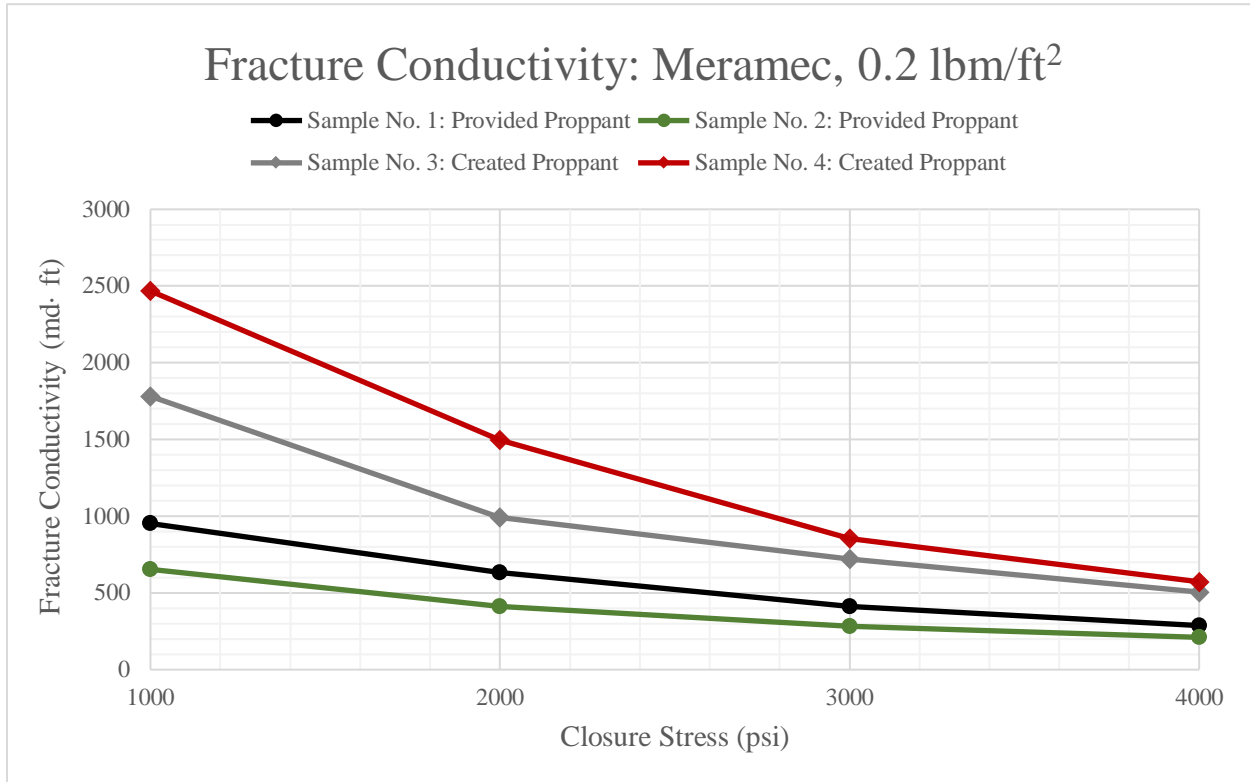
Figure 31. The calculated fracture conductivity values for the Meramec core samples.

For all samples, the fracture conductivity degreased as the closure stress increased. The plotted data for the samples propped by provided proppant exhibited a linear decline, while the samples propped by created proppant exhibited an exponential decline. Larger decreases in fracture conductivities at each closure stress interval occurred for the samples propped with created proppant than when provided proppant was used. The samples propped with the provided proppant behaved similarly to unpropped samples. However, regardless of fracture surface

conditions, the samples propped using the created proppant yielded higher conductivity values than the samples propped with the provided proppant. The created proppant proved to be more conductive due to the homogeneity of the grains.

Furthermore, during the experiment, the created proppant grains shifted and formed definitive channels. The channels formed allowed for more conductive nitrogen flow through the fracture. Mechanisms driving self-channeling proppant are fracture surface topography and flow rate. In some locations on the fracture surfaces, the top and bottom surfaces are in direct contact, while in other locations, proppant is packed between these surfaces. Loose proppant is then able to shift and rearrange from the peaked locations on the fracture surface to the "valley" locations.

The images in **Figure 32** were taken after the samples were removed from the Modified API cell. To ensure the proppant wasn't disturbed, the sample removal was done very carefully using the hydraulic pressure. In **Figure 32**, larger and more defined channels are depicted for the samples propped with the created proppant. These results support Guerra's (2019) theory that the self-channeling phenomenon is also related to the concentration and size of the proppant.

Additionally, the images taken after the experiments show where noticeable proppant crushing occurred. In some locations on the fracture surface where the proppant appears lighter in color, the proppant was crushed into finer grains. It was also more apparent in the laboratory setting. Proppant crushing occurs when the rock is stronger than the proppant. This crushing is a leading cause of proppant embedment.

Figure 32. Images of the proppant distribution on the fracture surfaces after the Meramec cores were tested: (a) Sample No. 1 with provided proppant; (b) Sample No. 2 with provided proppant; (c) Sample No. 3 with created proppant; (d) Sample No. 4 with created proppant.

3.3.2 Eagle Ford Core

Four samples made with Eagle Ford core extracted from an outcrop were tested; two with a provided 100-mesh proppant and two with a proppant made with the grains collected by the No. 120 sieve. The fracture conductivity values yielded, using **Eq. 16,** at each closure stress are plotted in **Figure 33.**
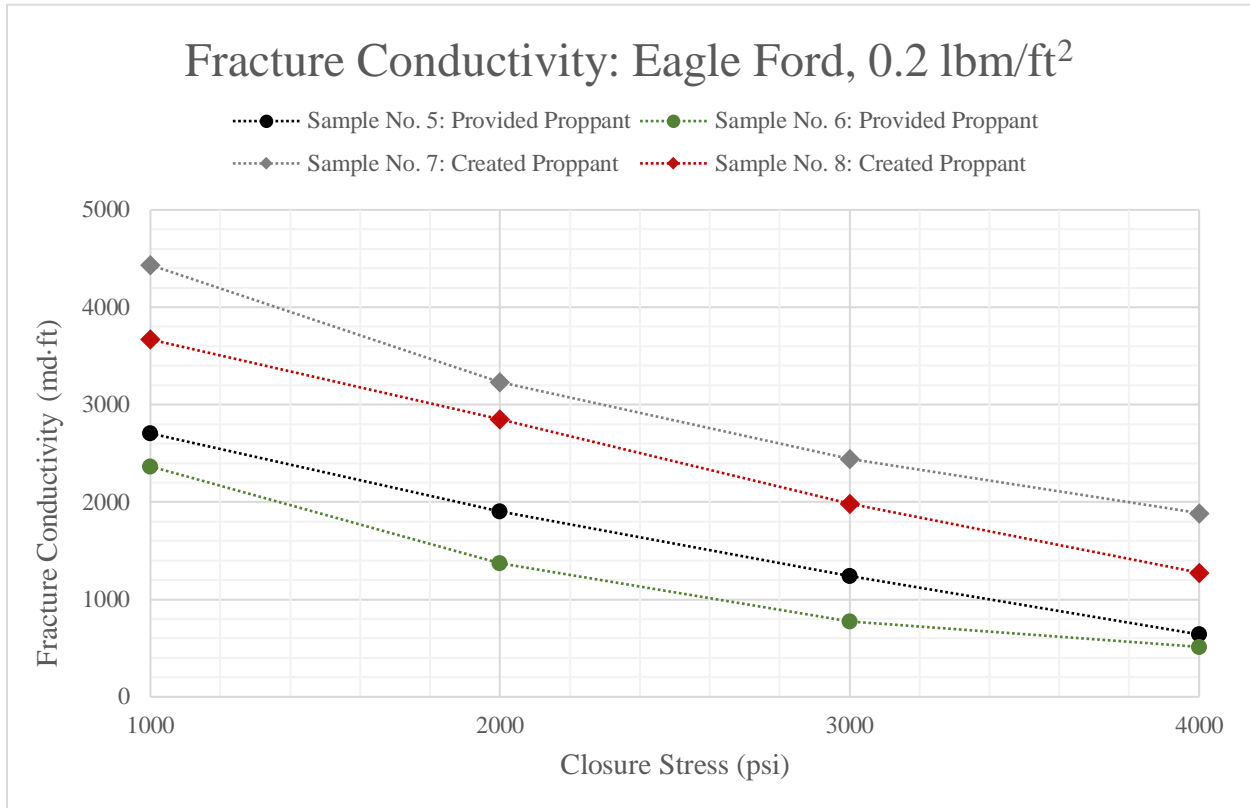
Figure 33. The calculated fracture conductivity values for the Eagle Ford samples.

Continuing the theme seen with the Meramec core results, the samples propped using the created proppant also yielded higher conductivity values. Proppant channeling also occurred more noticeably when the created proppant was used (**Figure 34**). Therefore, although two very different shale core were tested, proppant channeling occurred more predominately for a proppant with a uniform grain size distribution.
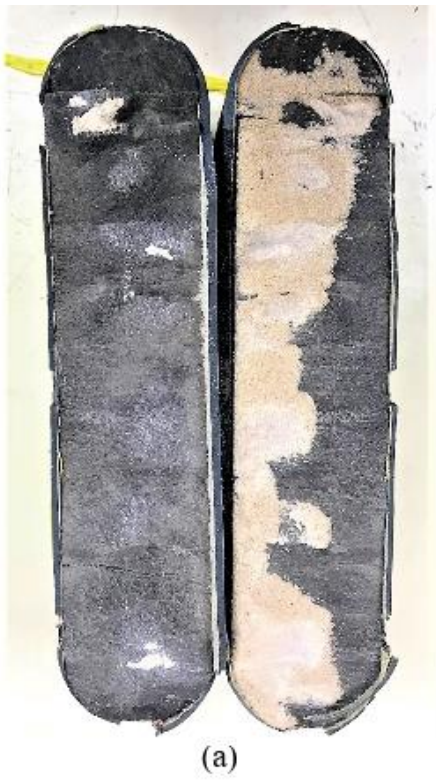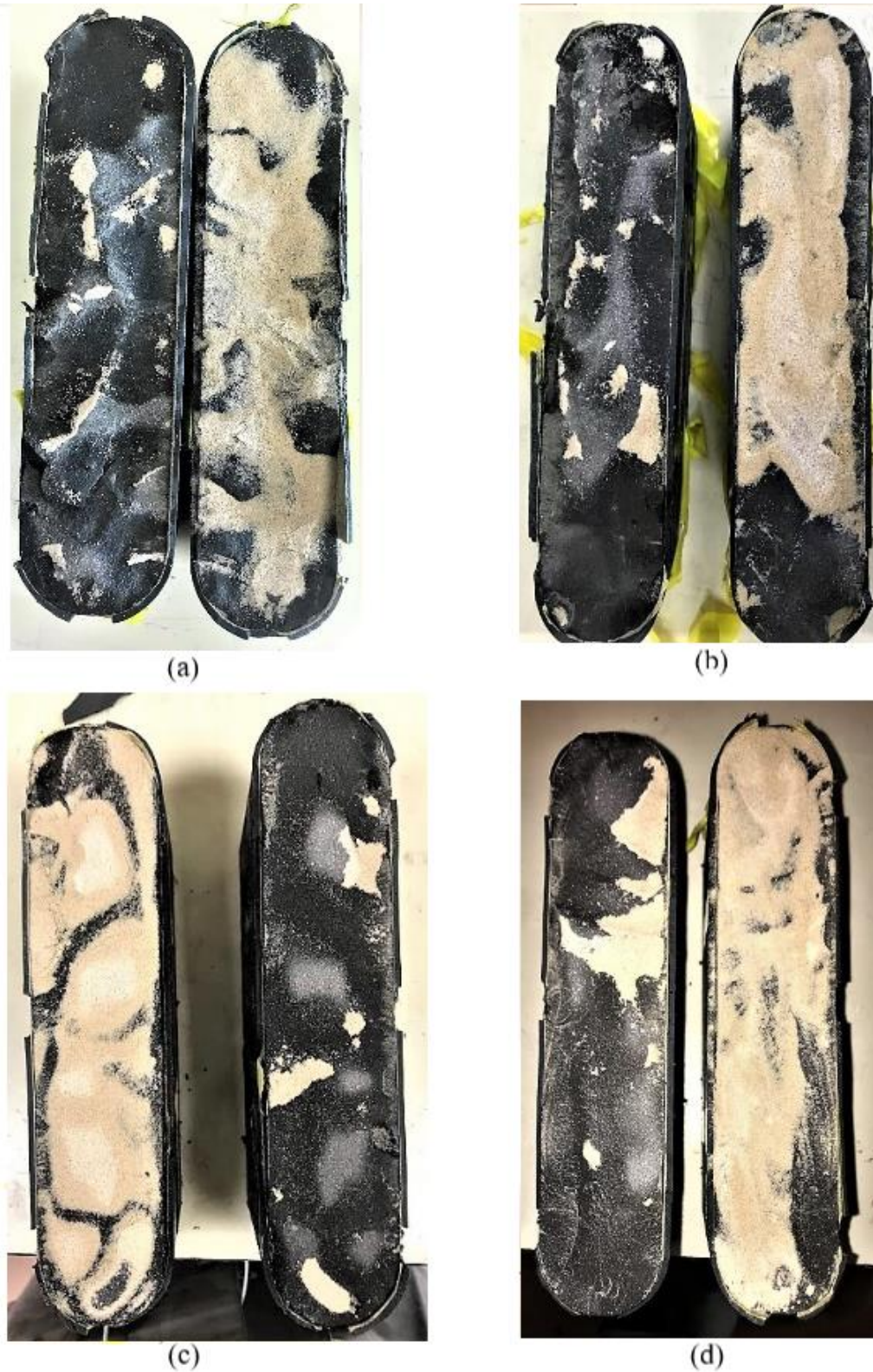
Figure 34. Images of the proppant distribution on the fracture surfaces after the Eagle Ford cores were tested: (a) Sample No. 5 with provided proppant; (b) Sample No. 6 with provided proppant; (c) Sample No. 7 with created proppant; (d) Sample No. 8 with created proppant.

3.3.3   Combined Results

Although the created proppant yielded higher conductivity values for both the Meramec and Eagle Ford cores, the values were not equivalent. In general, the Eagle Ford core consistently outperformed the Meramec core, regardless of the proppant used. The plot in **Figure 35** compares the fracture conductivity values calculated for the Meramec and Eagle Ford samples propped with the created proppant.
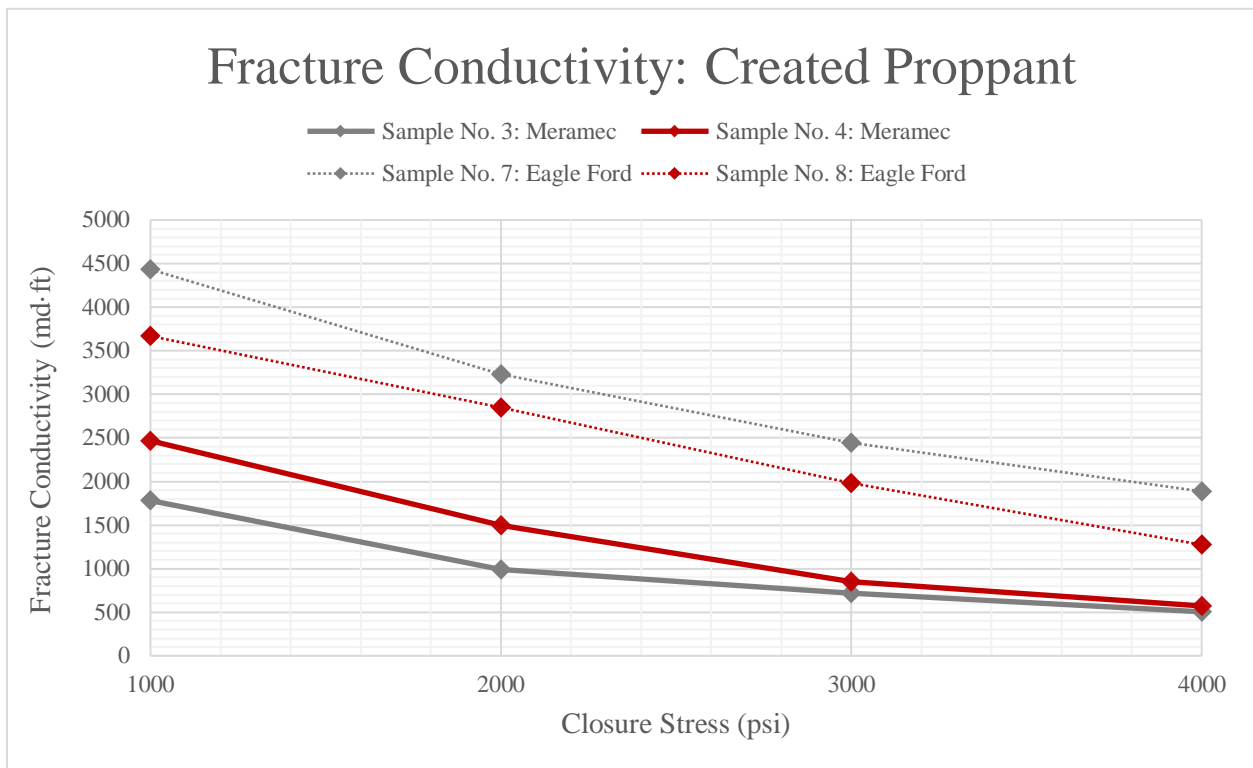
Figure 35. The results from the Meramec and Eagle Ford core experiments ran with the created proppant.

The conductivity values for the Eagle Ford core were both consistently higher than the values calculated for the Meramec core. This was also the case when the provided proppant was used. The plot in **Figure 36** compares the fracture conductivity values calculated for the Meramec and Eagle Ford samples propped with the provided proppant.
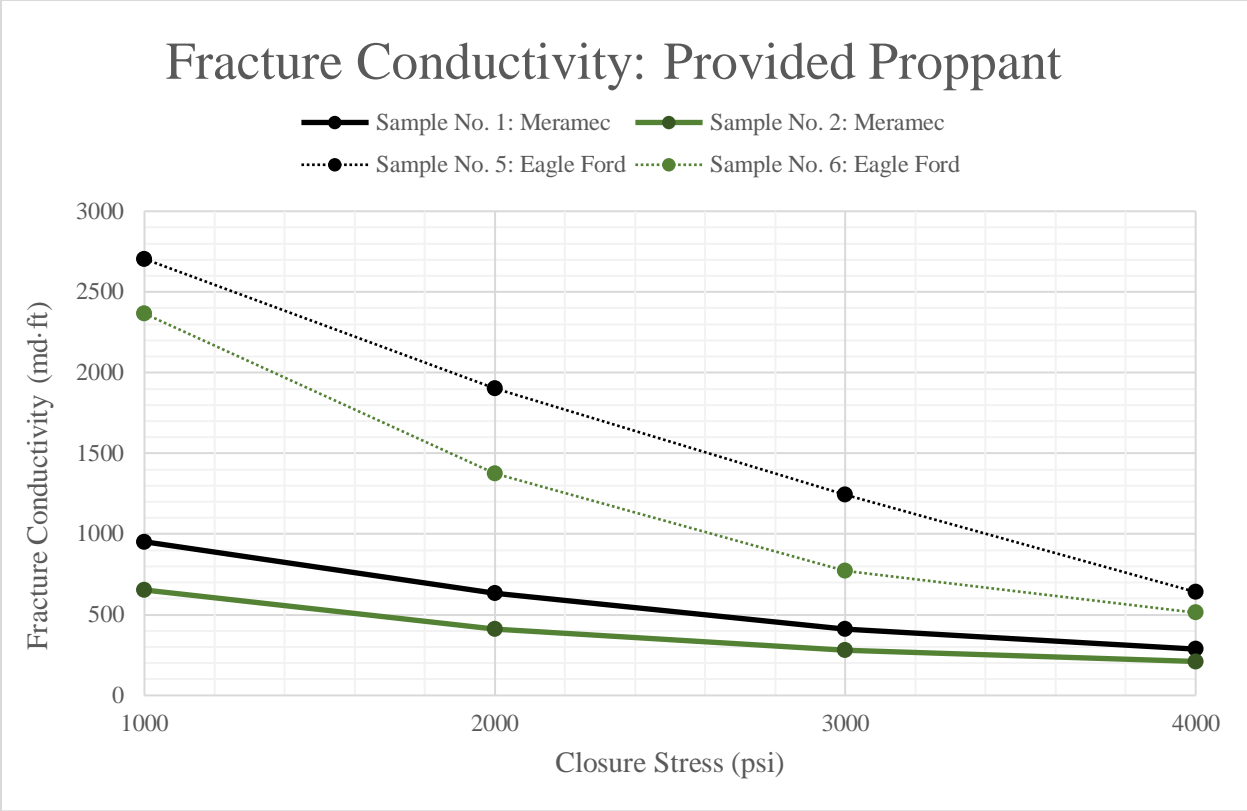
Figure 36. The results from the Meramec and Eagle Ford core experiments ran with the provided proppant.

The disparity between the Eagle Ford and Meramec fracture conductivity results can be attributed to the fracture surface topography and rock mineralogy. The Meramec fracture surfaces were jagged with discernable peaks, as indicated in **Figure 11** in Section 2.3.2. The Eagle Ford surfaces were smooth and curved like rolling hills (**Figure 12** in Section 2.3.2). The jagged and high peaked surfaces appeared to crush the proppant grains more aggressively and, as a result, reduce the fracture width.

Researchers from many engineering disciplines have proven the impact a surface can have on fluid flow. A jagged, non-uniform, or rough surface causes turbulent fluid flow. Smooth and uniform surfaces invoke laminar flow. Although, it can be argued that due to the small surface area of the fracture surfaces tested, laminar flow may have occurred for both fracture

surfaces. However, the peaked surfaces may have still restricted and disrupted the nitrogen flow allowing for turbulent flow characteristics, such as eddies, to occur. Fluid behavior for possible flow regimes is displayed in **Figure 37.**
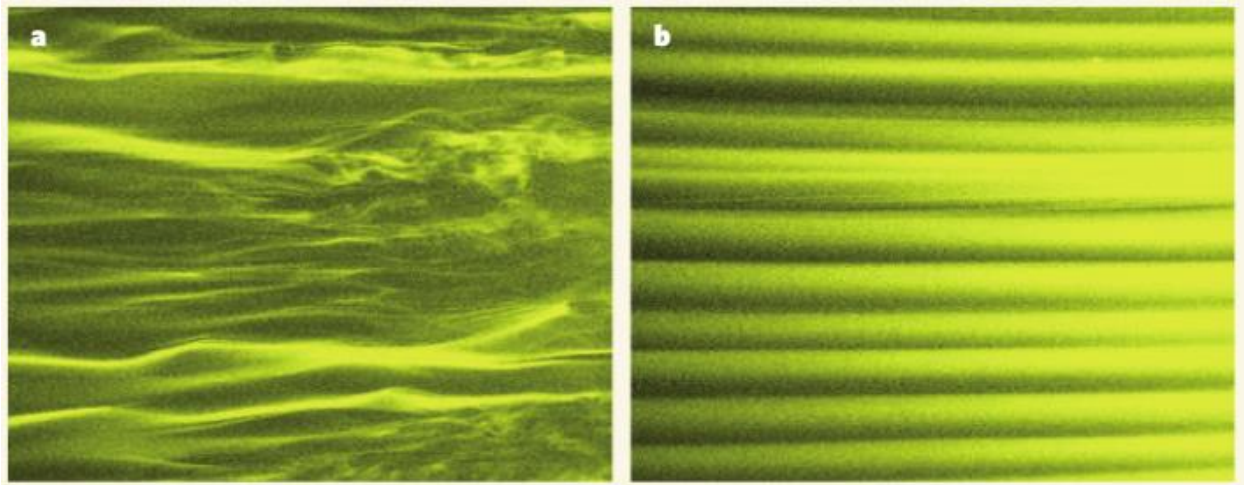
Figure 37. Flow patterns visualized by smoke: (a) laminar flow with minor turbulent flow; (b) laminar flow (Choi, 2006).

3.3.4 Additional Tests Ran

After seeing the results from the initial eight tests, the Eagle Ford core was re-tested with a proppant concentration or 0.1 lbm/ft². **Figure 38** compares the measured fracture conductivities for all Eagle Ford core experiments.
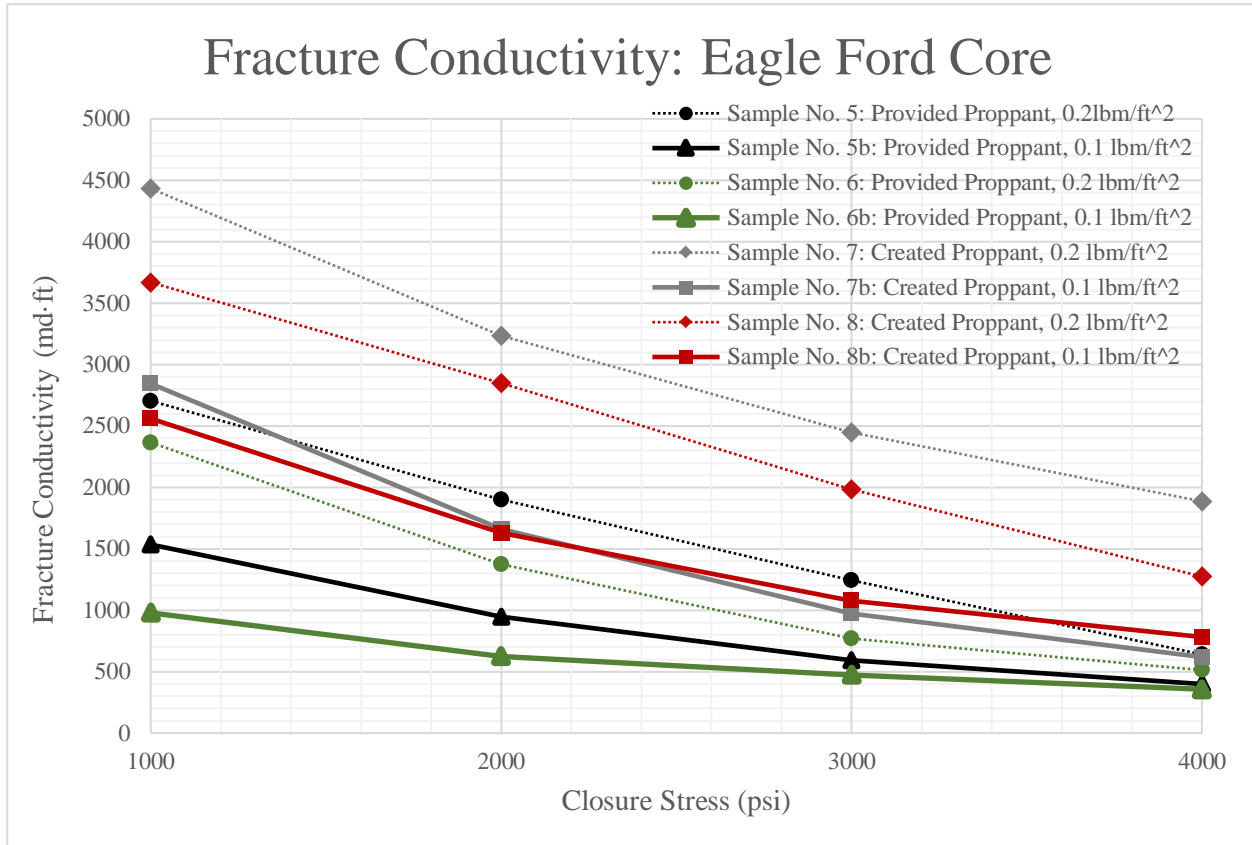
Figure 38. The calculated conductivity values for Eagle Ford core loaded with proppant concentrations of 0.1 lbm/ft² and 0.2 lbm/ft².

Understandably, the lower proppant concentrations yielded lower fracture conductivity values. Before exposing the sample to a closure stress, the fracture width for samples propped with a 0.1 lbm/ft² concentration is roughly half the fracture width of samples propped with a 0.2 lbm/ft² concentration. Fracture conductivity is directly proportional to fracture width. As a result,

the conductivity values measured for these different concentrations reflect the variations in fracture width.

4. CONCLUSIONS AND RECOMMENDATIONS

4.1 Conclusions

For this thesis, an extended study was conducted to determine the impact of proppant grain size distribution on fracture conductivity. Using the shale cores from the Meramec formation and an Eagle Ford outcrop, fracture conductivity values were measured for the core samples propped by a provided well distributed 100-mesh proppant and a created poorly distributed 100-mesh proppant. Although the main focus was on proppant, the fracture surface conditions and topography were also analyzed.

This thesis presented the methodology and experimental design used to quantify fracture conductivity. The pre-experimental work performed, such as proppant creation, sample preparation, surface profile scanning, was described and the procedures were listed. A post-experimental analysis of the results was done. Consistently, for different shale samples and proppant concentrations, a proppant with grains similar in size and shape yielded higher fracture conductivity values than a proppant with grains more non-uniformly distributed.

From the in-depth analysis of the results, the following conclusions were made:

1. Proppant with more uniformly distributed and spherical grains should result in higher conductivity, regardless of proppant concentration and fracture surface topography.

2. Proppant self-channeling is more likely to occur when the proppant grains are uniformly distributed.

3. Self-channeling can be controlled by proppant characteristics, but fracture surface topography can also promote self-channeling.

4. Proppant embedment is dependent on rock characteristics and proppant grain size distribution. The rock strength impacts proppant crushing and, thus, the embedment of fines. A more permeable shale is more susceptible to embedment. A proppant with a uniform grain size distribution may lead to increased proppant embedment, as opposed to a proppant with a non-uniform grain size distribution.

4.2 Limitations, Recommendations, and Future Work

A key limitation of this study was the quantity of samples tested. The validity of the previously presented conclusions can be strengthened only by performing more diverse experiments. Another limiting factor was the equipment used. Most of the equipment utilized for this thesis have been used by many other graduate students for many years. Although every measurement tool was calibrated, the age of the tool should be considered when planning future work.

The following are additional recommendations to consider for future work:

1. Using fresh core from the Eagle Ford outcrop and Meramec formation, test well distributed and poorly distributed 40/70-mesh proppant.

2. Because the fracture surface topography impacted the proppant behavior, the proppant can be tested under ideal conditions. Wylie (2018) presents the methodology for using steel plates to test and analyze proppant under ideal conditions. This style of testing purely measures the conductivity of the proppant and eliminates the inconsistencies between core sample fracture surfaces. Furthermore, proppant crushing can be quantified for both proppant types using this ideal method.

3. In the past, many researchers also considered the effect water damage can have on fracture conductivity in both the Meramec (Winner, 2018) and Eagle Ford (Guerra, 2019) formations. These experiments are more realistic and comparable to field conditions. A study can be done comparing the impact water damage has on the fracture conductivities measured for a core propped by poorly distributed 100-mesh to a core propped by well distributed 100-mesh.

4. Proppants are being modified and coated with adhesive agents to extend conductivity life by reducing the impact of fines migration on a proppant pack's conductivity (Lehman et al., 2003). This method could also be tested in the laboratory setting with the non-uniformly and uniformly distributed proppants.

REFERENCES

API RP-61. 1989. *Recommended Practices for Evaluating Short Term Proppant Pack Conductivity*. First Edition, October 1, 1989. Washington, D.C., U.S.A.: American Petroleum Institute.

ASTM Standard-C136M-19. 2019. *Standard Test Method for Sieve Analysis of Fine and Coarse Aggregates*. West Conshohocken, Pennsylvannia, U.S.A.: ASTM International.

Awoleke, O.O. 2013. Dynamic Fracture Conductivity - An Experimental Investigation Based on Factorial Analysis. PhD Dissertation, Texas A&M University, College Station, Texas, U.S.A. (May 2013).

Awoleke, O.O., Zhu, D., and Hill, A.D. 2016. New Propped-Fracture-Conductivity Models for Tight Gas Sands. *SPE Journal* **21** (5): 1,508-1,517. DOI: 10.2118/179743-PA.

Bureau of Reclamation. 2016. *Engineering Geology Field Manual* **1** (3).

Chipperfield, S. 2007. Overview: Hydraulic Fracturing. *Journal of Petroleum Technology* **59** (3): 44. DOI: 10.2118/0307-0044-JPT.

Choi, K.S. 2006. Fluid Dynamics: The rough with the smooth. *Nature* **440** (754). DOI: 10.1038/440754a.

Cooke Jr., C.E. 1973. Conductivity of Fracture Proppants in Multiple Layers. *Journal of Petroleum Technology* **25** (9): 1,101-1,107. DOI: 10.2118/4117-PA.

Cooke Jr., C.E. 1977. Fracturing with a High-Strength Proppant. *Journal of Petroleum Technology* **29** (10): 1,222-1,226. DOI: 10.2118/6213-PA.

Cronk, B.R., Gogri, M.P., Ortiz, J.E., Kalra, S., Cullen, A., Pranter, M.J., and Reza, Z.A. 2017. A Unified and Integrated Approach for Reservoir and Fluid Characterization Using Minimal Production and Well Data for the Mississippian Meramec Interval Within the STACK Play of Oklahoma. Paper presented at the SPE Liquids-Rich Basins Conference, Midland, Texas, U.S.A., 13-14 September. Society of Petroleum Engineers. DOI: 10.2118/187497-MS.

Daniel, G. and White, J. 1980. Fundamentals of Fracturing. Paper presented at SPEC Cotton Valley Symposium, Tyler, Texas, U.S.A., 21 May. Society of Petroleum Engineers. DOI: 10.2118/9064-MS

Donovan, A.D., Staerker, T.S., Pramudito, A., Li, W., Corbett, M.J., Lowery, C.M., Romero, A.M., and Gardner, R.D. 2012. The Eagle Ford Outcrops of West Texas: A Laboratory for Understanding Heterogeneities within Unconventional Mudstone Reservoirs. *CGAGS Journal* **1**: 162-185.

Duenckel, R.J., Barree, R.D., Drylie, S., O'Connell, L.G., Abney, K.L., Conway, M.W., Moore, N., and Chen, F. 2017. Proppants – What 30 Years of Study Has Taught Us. Paper presented at SPE Annual Technical Conference and Exhibition, San Antonio, Texas, U.S.A. 9-11 October. Society of Petroleum Engineers. DOI: 10.2118/187451-MS

Enriquez, O. 2016. A Comprehensive Study of the Eagle Ford Shale Fracture Conductivity. MS Thesis, Texas A&M University, College Station, Texas, U.S.A. DOI: 10.2118/181858-PA.

Enriquez, O., Knorr, A., Zhu, D., and Hill, A.D. 2016. Relationships between Mechanical Properties and Fracturing Conductivity for the Eagle Ford Shale. Paper presented at the SPE Asia Pacific Hydraulic Fracturing Conference, Beijing, China, 24-26 August. Society of Petroleum Engineers. DOI: 10.2118/181858-MS.

Gomaa, A.M., Hudson, H., Nelson, S., and Brannon, H. 2016. Hydraulic Fracturing Treatment Design Considerations for Effective Proppant Pillar Construction. Paper presented at the SPE Annual Technical Conference and Exhibition, Dubai, U.A.E., 26-28 September. Society of Petroleum Engineers. DOI: 10.2118/181508-MS.

Guerra, J. 2019. Fracture Conductivity Behavior in Shale Formations. PhD Dissertation, Texas A&M University, College Station, Texas, U.S.A. (August 2019).

Guerra, J., Zhu. D., and Hill, A.D. 2018. Impairment of Fracture Conductivity in the Eagle Ford Shale Formation. Paper presented at the SPE Hydraulic Fracture Technology Conference and Exhibition, The Woodlands, Texas, U.S.A., 24-26 January. Society of Petroleum Engineers. DOI: 10.2118/184857-MS.

Kamenov, A.N. 2013. The Effect of Proppant Size and Concentration on Hydraulic Fracture Conductivity in Shale Reservoirs. MS Thesis, Texas A&M University, College Station, Texas, U.S.A. (May 2013).

Larsen, D.G. and Smith, L.J. 1985. New Conductivity Found in Angular Blends of Fracturing Sand. Paper presented at the SPE Production Operations Symposium, Oklahoma City, Oklahoma, U.S.A., 10-12 March. Society of Petroleum Engineers. DOI: 10.2118/13814-MS.

Lee, D.S., Herman, J.D., Elsworth, D., Kim, H.T., and Lee, H.S. 2010. A Critical Evaluation of Unconventional Gas Recovery from the Marcellus Shale, Northeastern United States. *KSCE Journal of Civil Engineering* **15:** 679-687. DOI: 10.1007/s12205-011-0008-4.

Mittal, A., Rai, C. S. and Sondergeld, C. H. 2017. A Study of Propped-Fracture Conductivity: Impairment Mechanisms Under Laboratory Conditions. Presented at the SPWLA 58th Annual Symposium, Oklahoma City, Oklahoma, U.S.A., 17-21 June. Society of Petroleum Engineers. SPWLA-2017-CC.

Mittal, A., Rai, C. S. and Sondergeld, C. H. 2018. Proppant-Conductivity Testing Under Simulated Reservoir Conditions: Impact of Crushing, Embedment, and Diagenesis on Long-Term Production in Shales. *SPE Journal* **23** (4). DOI: 10.2118/191124-PA.

Montgomery, C.T. and Smith, M.B. 2010. Hydraulic Fracturing: History of an Enduring Technology. *Journal of Petroleum Technology* **62** (12): 26-32. DOI: 10.2118/1210-0026-JPT.

Palisch, T.T., Vincent, M., and Handren, P.J. 2010. Slickwater Fracturing: Food for Thought. *SPE Production & Operations* **25** (3): 327-344. DOI: 10.2118/115766-PA.

Raimbay, A., Babadagli, T., Kuru, E., and Develi, K. 2015. Quantitative and Visual Analysis of Proppant Transport in Rough Fractures and Aperture Stability. Paper presented at the SPE Hydraulic Fracturing Technology Conference, The Woodlands, Texas, U.S.A., 3-5 February. Society of Petroleum Engineers. DOI: 10.2118/173385-MS.

Selley, R.C. *Elements of Petroleum Geology*. Second Edition, October 2, 1997. San Diego, California, U.S.A.: Academic Press.

University of Nebraska Omaha. 2020. Distance Learning Module 15 – Ground Water. International Programs – Center of Afghanistan Studies.

U.S. Department of Agriculture. 2012. *National Engineering Handbook, Chapter 3: Engineering Classification of Earth Materials*. 210-VI-NEH, Amend. 55.

U.S. Energy Information Administration. 2020. Drilling Productivity Report: For Petroleum and Other Liquids. (March 2020).

Vangla, P. and Latha, G.M. 2015. Influence of Particle Size on the Friction and Interfacial Shear Strength of Sands of Similar Morphology. *International Journal of Geosynthetics and Ground Engineering* **1** (6). DOI: 10.1007/s40891-014-0008-9.

Winner, R. 2018. A Study on the Effect of Water Damage to Fracture Conductivity in the Meramec Shale. MS Thesis, Texas A&M University, College Station, Texas, U.S.A. (August 2018).

Wylie, K. 2018. Experimental Evaluation of Novel Proppants for Use in Hydraulic Fracturing of Unconventional Reservoirs. MS Thesis, Texas A&M University, College Station, Texas, U.S.A. (May 2018).

Zhang, J. 2014. Creation and Impairment of Hydraulic Fracturing Conductivity in Shale Formations. PhD Dissertation, Texas A&M University, College Station, Texas, U.S.A. (August 2014).

Zhang, J., Ouyang, L., Hill, A.D., and Zhu, D. 2014. Experimental and Numerical Studies of Reduced Fracture Conductivity Due to Proppant Embedment in Shale Reservoirs. Paper

presented at the SPE Annual Technical Conference and Exhibition, Amsterdam, The Netherlands, 27-29 October. Society of Petroleum Engineers. DOI: 10.2118/170775-MS.

Zhang, J., Zhu, D., and Hill, A.D. 2015. Water-Induced Fracture Conductivity Damage in Shale Formations. Paper presented at the SPE Hydraulic Fracturing Technology Conference, The Woodlands, Texas, U.S.A., 3-5 February. Society of Petroleum Engineers. DOI: 10.2118/173346-MS.

Zhu, D. and Hill, A.D. 2013. Conductivity of Complex Fracturing in Unconventional Shale Reservoirs. Technology Assessment: 11122-07-TAMU-Zhu.

Zinni, Y. 2017. Geology: Difference Between Quartz and Calcite. *Sciencing*. Leaf Group Media.

APPENDIX A

STRESS VERSUS STRAIN ANALYSIS

The GTCS load frame and acquisition software were also utilized to perform preliminary stress and strain calculations. Zhang (2014) performed this procedure to measure the strain of the shale. In this experiment, a combined strain of the shale and spacers were measured and the sample was analyzed as a whole.

The laser profilometer was used to scan the fracture surfaces before and after the loadings. The scans collected after the loadings were used for the volume change quantities in Section 3.2.1.

To begin the analysis, each sample was centered under the load frame between two pistons. The bottom piston was attached to a support base (**Figure 38**). Before the closure stresses were applied to the samples, the initial axial displacements were recorded. The samples were loaded to 1000 psi, 2000 psi, 3000 psi, and 4000 psi. At each loading interval, the axial displacement was recorded. Strain experienced by each sampled was quantified using the change in axial displacement.

Figure 39. Laboratory setup used to calculate stress and strain measurements.

The following plots (**Figure 39 and 40**) display the relationship between the closure

stress and strain applied to the samples. Although two different types of shale were analyzed, the
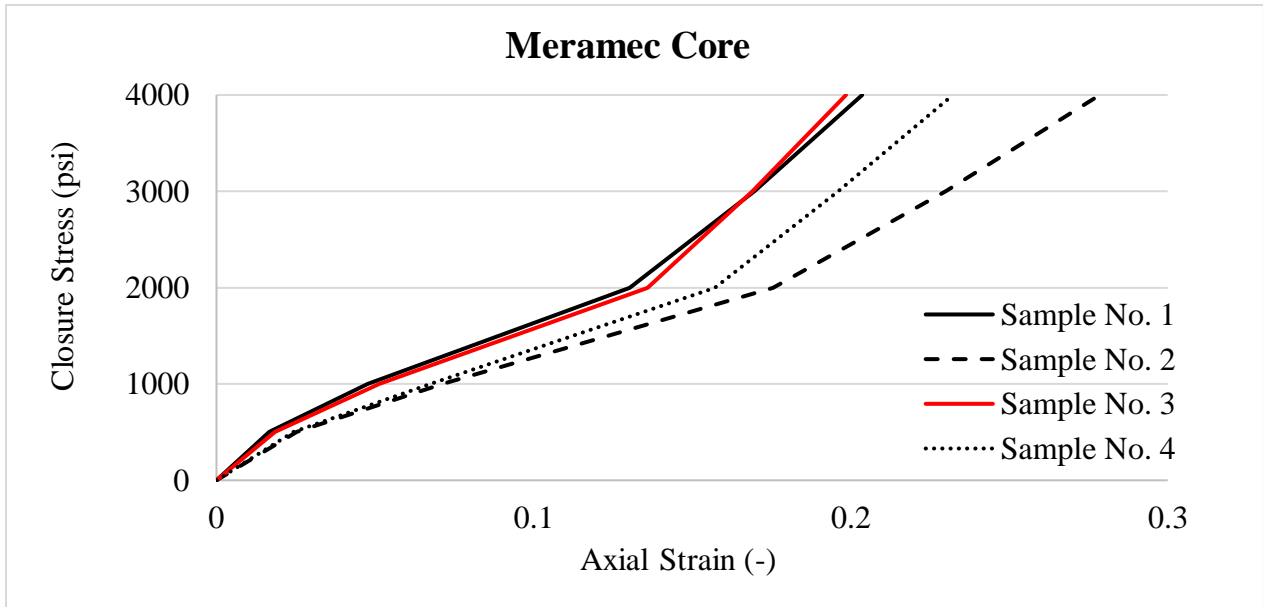
respective strain values were very similar.

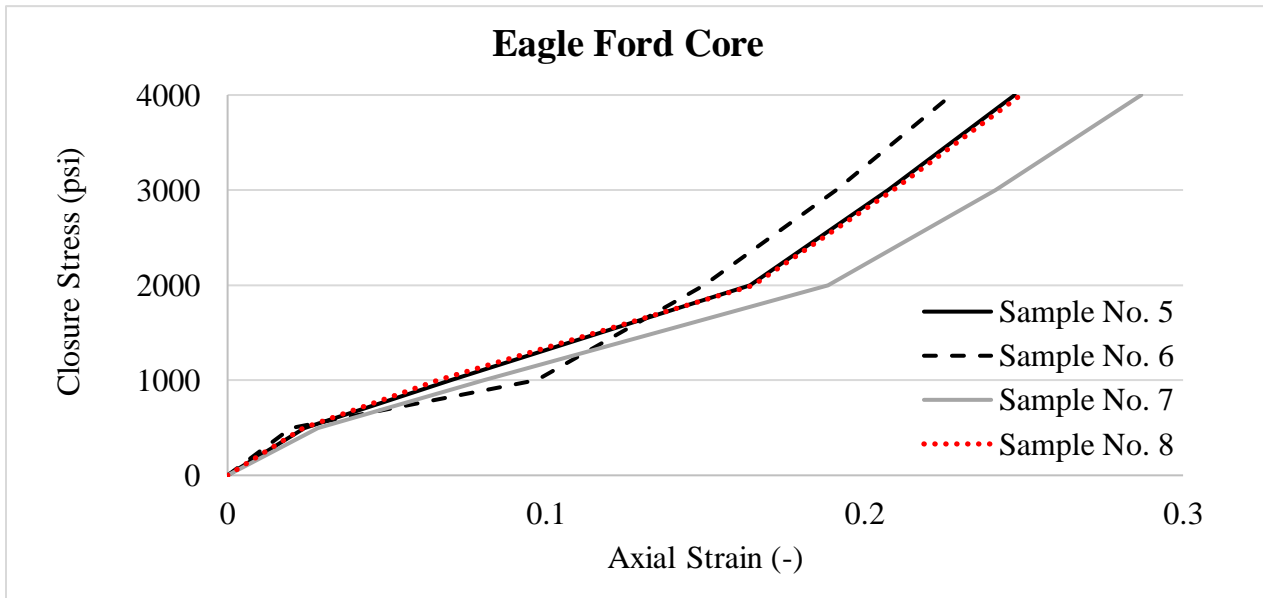**Figure 40.** Stress vs. strain relationship for the Meramec Core.

Figure 41. Stress vs. strain relationship for the Eagle Ford core.